



# **NAVAL POSTGRADUATE SCHOOL**

**MONTEREY, CALIFORNIA**

## **THESIS**

**TRANSPORT IMAGING FOR THE STUDY OF  
NANOWIRES AND RELATED NANOSTRUCTURES**

by

Ang Goon Hwee

December 2007

Thesis Advisor:  
Co-Advisor:

Nancy M. Haegel  
James Luscombe

**Approved for public release; distribution is unlimited**

THIS PAGE INTENTIONALLY LEFT BLANK

<b>REPORT DOCUMENTATION PAGE</b>			<i>Form Approved OMB No. 0704-0188</i>	
Public reporting burden for this collection of information is estimated to average 1 hour per response, including the time for reviewing instruction, searching existing data sources, gathering and maintaining the data needed, and completing and reviewing the collection of information. Send comments regarding this burden estimate or any other aspect of this collection of information, including suggestions for reducing this burden, to Washington headquarters Services, Directorate for Information Operations and Reports, 1215 Jefferson Davis Highway, Suite 1204, Arlington, VA 22202-4302, and to the Office of Management and Budget, Paperwork Reduction Project (0704-0188) Washington DC 20503.				
<b>1. AGENCY USE ONLY (Leave blank)</b>		<b>2. REPORT DATE</b> December 2007	<b>3. REPORT TYPE AND DATES COVERED</b> Master's Thesis	
<b>4. TITLE AND SUBTITLE</b> Transport Imaging for the Study of Nanowires and Related Nanostructures			<b>5. FUNDING NUMBERS</b>	
<b>6. AUTHOR(S)</b> Ang, Goon Hwee				
<b>7. PERFORMING ORGANIZATION NAME(S) AND ADDRESS(ES)</b> Naval Postgraduate School Monterey, CA 93943-5000			<b>8. PERFORMING ORGANIZATION REPORT NUMBER</b>	
<b>9. SPONSORING /MONITORING AGENCY NAME(S) AND ADDRESS(ES)</b> National Science Foundation			<b>10. SPONSORING/MONITORING AGENCY REPORT NUMBER</b> DMR-0526330	
<b>11. SUPPLEMENTARY NOTES</b> The views expressed in this thesis are those of the author and do not reflect the official policy or position of the Department of Defense or the U.S. Government.				
<b>12a. DISTRIBUTION / AVAILABILITY STATEMENT</b> Approved for public release; distribution is unlimited			<b>12b. DISTRIBUTION CODE</b>	
<b>13. ABSTRACT</b> <p>The goals of this thesis are to demonstrate the operation of a near-field scanning microscope (NSOM) inside a scanning electron microscope (SEM) to collect spatially resolved luminescence and to image transport on nano-scale structures, particularly nanowires. The SEM is used to generate localized charge and the NSOM is used to observe the motion of the excess charge due to diffusion and/or drift via its recombination emission. This will allow direct determination of transport parameters, such as minority carrier mobility and lifetime, that are key to the performance of LEDs, lasers and bipolar devices.</p> <p>For nano-structures such as nanowires, device sizes are commonly less than 100 nm. The resolution in a standard optical microscope is diffraction limited and hence resolution of luminescence from individual devices requires collection of light in the near field limit. An atomic force microscope (AFM/NSOM) has been installed in the SEM to allow for simultaneous near-field optical collection with an electron beam for charge generation. The work in this thesis has observed CL luminescence from ZnO nanowires using normal SEM-OM and analyzed the spectra. In addition, the work has demonstrated successful AFM/NSOM operation within the SEM. Light is collected from both GaAs heterostructures and single ZnO nanowires and control experiments have been performed. Challenges for transport imaging in SEM have been identified</p> <p>Finally, a suggestion for further work is to specifically image charge motion along a single wire, including electric field mapping in these nanoscale, low dimensional structures. These nanoscale wires are poised to revolutionize solid state devices in the near future and direct measurements of key electronic parameters will be required.</p>				
<b>14. SUBJECT TERMS</b> Diffusion, Direct Transport Imaging, Minority Carrier Lifetime, Minority Carrier Mobility, Zinc Oxide Nanowires, Zinc Oxide Nanostructures, Cathodoluminescence, Nearfield Scanning Optical Microscope, Atomic Force Microscope.			<b>15. NUMBER OF PAGES</b> 105	
			<b>16. PRICE CODE</b>	
<b>17. SECURITY CLASSIFICATION OF REPORT</b> Unclassified	<b>18. SECURITY CLASSIFICATION OF THIS PAGE</b> Unclassified	<b>19. SECURITY CLASSIFICATION OF ABSTRACT</b> Unclassified	<b>20. LIMITATION OF ABSTRACT</b> UU	

Standard Form 298 (Rev. 8-98)  
Prescribed by ANSI Std. Z39.18

THIS PAGE INTENTIONALLY LEFT BLANK

**Approved for public release; distribution is unlimited**

**TRANSPORT IMAGING FOR THE STUDY OF NANOWIRES AND RELATED  
NANOSTRUCTURES**

Ang Goon Hwee  
Major, Singapore Navy  
B.Eng. (Hons), University of Leeds (UK), 1999

Submitted in partial fulfillment of the  
requirements for the degree of

**MASTER OF SCIENCE IN APPLIED PHYSICS**

from the

**NAVAL POSTGRADUATE SCHOOL  
December 2007**

Author: Ang Goon Hwee

Approved by: Nancy M. Haegel  
Thesis Advisor

James Luscombe  
Co-Advisor

James Luscombe  
Chairman, Department of Physics

THIS PAGE INTENTIONALLY LEFT BLANK

## ABSTRACT

The goals of this thesis are to demonstrate the operation of a near-field scanning microscope (NSOM) inside a scanning electron microscope (SEM) to collect spatially resolved luminescence and to image transport on nano-scale structures, particularly nanowires. The SEM is used to generate localized charge and the NSOM is used to observe the motion of the excess charge due to diffusion and/or drift via its recombination emission. This will allow direct determination of transport parameters, such as minority carrier mobility and lifetime, that are key to the performance of LEDs, lasers and bipolar devices.

For nano-structures such as nanowires, device sizes are commonly less than 100 nm. The resolution in a standard optical microscope is diffraction limited and hence resolution of luminescence from individual devices requires collection of light in the near field limit. An atomic force microscope (AFM/NSOM) has been installed in the SEM to allow for simultaneous near-field optical collection with an electron beam for charge generation. The work in this thesis has observed CL luminescence from ZnO nanowires using normal SEM-OM and analyzed the spectra. In addition, the work has demonstrated successful AFM/NSOM operation within the SEM. Light is collected from both GaAs heterostructures and single ZnO nanowires and control experiments have been performed. Challenges for transport imaging in SEM have been identified.

Finally, a suggestion for further work is to specifically image charge motion along a single wire, including electric field mapping in these nanoscale, low dimensional structures. These nanoscale wires are poised to revolutionize solid state devices in the near future and direct measurements of key electronic parameters will be required.

THIS PAGE INTENTIONALLY LEFT BLANK

## TABLE OF CONTENTS

I.	INTRODUCTION.....	1
A.	BACKGROUND .....	1
B.	MILITARY RELEVANCE .....	3
C.	THESIS OVERVIEW .....	3
II.	TRANSPORT IMAGING OF NANOWIRES - THEORY .....	5
A.	TRANSPORT THEORY .....	5
1.	Luminescence Phenomena.....	5
2.	Cathodoluminescence .....	7
3.	Carrier Transport .....	11
4.	Transport Imaging .....	13
B.	NANOSTRUCTURES AND NANOWIRES .....	13
1.	Nanowire Applications .....	13
2.	Fabrication of Nanowires .....	14
3.	Properties of Nanowires.....	18
C.	MODELING TRANSPORT IN THE ONE DIMENSIONAL LIMIT .....	20
III.	EXPERIMENTAL TECHNIQUES.....	23
A.	THE SCANNING ELECTRON MICROSCOPE (SEM) .....	23
1.	The Cathodoluminescence System .....	25
2.	Optical Microscope and CCD Camera .....	26
3.	The Diffraction Limit.....	28
B.	ATOMIC FORCE MICROSCOPE (AFM) AND NEAR FIELD SCANNING OPTICAL MICROSCOPE (NSOM) .....	30
1.	AFM.....	30
2.	NSOM .....	32
C.	DATA EXTRACTION AND ANALYSIS .....	34
1	Obtaining the Diffusion Length from Experimental Data ...	35
IV.	STUDY OF NANOWIRES.....	37
A.	IMAGING OF ZNO NANOWIRES .....	37
1.	CL Measurements.....	37
2.	Effect of Size on ZnO Nanowire Luminescence .....	39
3.	CL Measurements with Band Pass Filter .....	41
4.	OM Measurements .....	43
B.	MODELING ZINC OXIDE NANOWIRES .....	48
V.	INSTALLATION AND OPERATION OF AFM/NSOM .....	51
A.	OPTIMIZATION OF AFM/NSOM SCAN QUALITY.....	51
1.	Tip Integration Time .....	52
2.	Upper Scanner and Lower Scanner .....	53
3.	Amplitude Feedback Vs Phase Feedback .....	54
4.	Feedback PID Controller .....	55
B.	AFM/ NSOM CALIBRATION .....	56

C.	TOPOGRAPHICAL AND OPTICAL RESOLUTION .....	57
D.	TIP AND CHARGES INTERACTION.....	59
VI.	IMAGING OF NANOWIRES USING AFM AND NSOM.....	61
A.	NANOSCALE FEATURES OF ZINC OXIDE WIRES. ....	61
B.	“FIRST LIGHT” .....	62
C.	FIRST DIFFUSION LENGTH MEASUREMENT USING NSOM .....	65
VII.	IMAGING OF OTHER WIRES .....	69
A.	SILICON NANOWIRES.....	69
1.	Si Nanowire Bridges in Microtrenches .....	69
2.	Si Nanowires Made from CVD.....	70
VIII.	CONCLUSIONS AND SUGGESTIONS FOR FURTHER RESEARCH .....	73
A.	CONCLUSION .....	73
B.	SUGGESTIONS FOR FURTHER RESEARCH .....	74
1	New NSOM Tips .....	74
2.	Applied Electric Field Studies .....	74
3.	Quantum Mechanical and Other Effects in 1D Transport... 75	
	ANNEX – MATLAB PROGRAMS FOR DATA ANALYSIS.....	77
	LIST OF REFERENCES.....	83
	INITIAL DISTRIBUTION LIST .....	87

## LIST OF FIGURES

Figure 1.	Band diagrams of (left) direct band gap, (right) indirect band gap materials.....	6
Figure 2.	Electron range vs electron beam energy for Si, GaAs and ZnO.....	8
Figure 3.	Penetration depths, according to the depth-dose function for ZnO at various beam energies. ....	9
Figure 4.	Pear shape excitation volume in bulk samples.....	10
Figure 5.	Cluster of nanowires produced by VLS mechanism (sample A).....	15
Figure 6.	Optical image of a ZnO wire across a 5 $\mu\text{m}$ gap (sample B). ....	16
Figure 7.	Schematic illustration of bridged nanowire fabrication (from [2]). ....	17
Figure 8.	Si wires bridging the trenches. ....	17
Figure 9.	HP nanowires at 50000X. (a) CVD 893, (b) CVD 895, (c) CVD 904..	18
Figure 10.	Energy between states/kT (Energy of $n=2$ to $n=1$ ) of ZnO, GaAs and Si as a function of quantum well width (aka diameter of nanowires) for $T=300\text{K}$ . ....	20
Figure 11.	Numerical calculations of the steady state model: (a) Normalized intensity as a function of $L$ , $m=8$ , $E=0$ . (b) Normalized intensity as a function of $E$ , $m=8$ , $L=3.5 \mu\text{m}$ . (c) Normalized intensity as a function of sidelength, $L=3.5 \mu\text{m}$ , $E=0$ . (d) Expansion plot of (c).....	22
Figure 12.	OM and spectrometer connected to JEOL 840A SEM. ....	23
Figure 13.	'Picture' mode micrograph of ZnO nanowires on Si substrate (sample 'D') at working distance of 9 mm, $6 \times 10^{-11} \text{ A}$ , 20 keV, 11000X. ....	25
Figure 14.	AC transport imaging (a) toward the fringe field (b) and in the center region of the parallel plate geometry. Each image is 330 (w) $\mu\text{m}$ x 250 (h) $\mu\text{m}$ . Electron-beam was $3 \times 10^{-8} \text{ A}$ and 20 keV (from [22]). ...	26
Figure 15.	Optical resolution at different wavelength with $\text{NA} = 0.95$ . ....	27
Figure 16.	A simulated Airy pattern (normalized arbitrary units) (from [26]). ....	28
Figure 17.	(a) Single resolvable sources, (b) Two sources still resolvable at $2R$ apart, and (c) Two sources barely resolvable at $R$ apart (from [27])...	30
Figure 18.	AFM topography image of a calibration grid 50 $\mu\text{m}$ x 50 $\mu\text{m}$ . The periodicity of the grid is 10 $\mu\text{m}$ and the islands are 100 nm tall. ....	32
Figure 19.	(a) Nanonics Multiview 2000 AFM/NSOM flat scanners (from [29]), (b) Optical image of the NSOM tip.....	33
Figure 20.	(Left) Fixed electron beam and probe, sample moves in x-y plane. (right) fixed electron beam and sample, probe moves in x-y plane. ...	34
Figure 21.	SEM micrograph (left) and CL image (right) of a group of ZnO nanowires on both Si and metal regions at 5000X. ....	37
Figure 22.	CL spectra of ZnO nanowire and its substrate. ....	38
Figure 23.	PL spectra obtained from ZnO wires of three different sizes (from [4]). ....	40
Figure 24.	CL intensity spectra of a ZnO wire approximately 500 nm in diameter .....	41

Figure 25.	SEM micrograph (left) and CL image (right) of a single ZnO wire at 5000X.....	41
Figure 26.	SEM micrograph (left) and CL image (right) with $\lambda = 380$ nm for a ZnO wire (5000X).....	42
Figure 27.	CL image panchromatic (left) and with $\lambda = 380$ nm (right) at 15000X.....	43
Figure 28.	SEM micrograph (left) and OM scan mode image (right) on ZnO wires at 5000X.....	43
Figure 29.	OM images of single ZnO wires with 380-bandpass filter (the 2 left images are SEM micrographs of the corresponding wires) at 8000X.....	44
Figure 30.	SEM scan and spot modes images of 2 different wires (Probe current = $1 \times 10^{-10}$ A, 20 keV).....	45
Figure 31.	Intensity distribution along the wire (spot mode) with varying electron beam probe current. ....	46
Figure 32.	Intensity distribution along and across the wire at probe current $6 \times 10^{-10}$ A.....	47
Figure 33.	Simulated recombination intensity profiles of a 1-D material, $L=0.3$ $\mu\text{m}$ , $m = 8000 \mu\text{m}^{-1}$ (generation region side length = 100 nm), for several values of electric field.....	49
Figure 34.	(a) AFM topography image of a GaAs structure 40 $\mu\text{m}$ x 40 $\mu\text{m}$ . (b) the corresponding NSOM image. ....	51
Figure 35.	AFM scans on the edge of a 100 nm tall structure 20 $\mu\text{m}$ x 20 $\mu\text{m}$ . (a) tip integration time 10 ms, (b) 20 ms.....	52
Figure 36.	AFM scans of ZnO wire 10 $\mu\text{m}$ x 5 $\mu\text{m}$ (a) top scanner, (b) bottom scanner.....	53
Figure 37.	AFM scan on a solar cell contact edge about 200 nm tall (30 $\mu\text{m}$ x 30 $\mu\text{m}$ ), using top x-y scanners and bottom in z feedback.....	54
Figure 38.	AFM scans on calibration grid 20 $\mu\text{m}$ x 20 $\mu\text{m}$ , with feature height of 100 nm, (a) using magnitude feedback, (b) using phase feedback. ....	55
Figure 39.	Effect of tuning the AFM PID feedback. (a) Initial AFM image of a wire 20 $\mu\text{m}$ x 18 $\mu\text{m}$ , (b) AFM image 15 $\mu\text{m}$ x 15 $\mu\text{m}$ with optimized PID feedback. ....	56
Figure 40.	AFM scans calibration grid (a) 50 $\mu\text{m}$ x 50 $\mu\text{m}$ , (b) 20 $\mu\text{m}$ x 20 $\mu\text{m}$ . ....	57
Figure 41.	Illustration of an NSOM tip scanning over an ideal edge.....	58
Figure 42.	Topography and NSOM line scan of a forward biased solar cell. ....	59
Figure 43.	SEM image of an NSOM tip on the tuning fork. Note the distorted structure due to charging.....	60
Figure 44.	(a) SEM image of ZnO wire cluster, (b) Image showing some interaction between the wires and substrate .....	61
Figure 45.	AFM topography image of ZnO nanowires. (a) 10 $\mu\text{m}$ x 10 $\mu\text{m}$ , (b) 5 $\mu\text{m}$ x 5 $\mu\text{m}$ , and (c) zoomed down to 1 $\mu\text{m}$ x 1 $\mu\text{m}$ . ....	62
Figure 46.	NSOM signals of a group of ZnO nanowires (20 $\mu\text{m}$ x 20 $\mu\text{m}$ ) and representative horizontal intensity line scans. ....	63
Figure 47.	SEM image of the area being scanned for NSOM signal (10000X)....	63

Figure 48.	NSOM signals of a 2nd group of ZnO nanowires (15 $\mu\text{m}$ x 15 $\mu\text{m}$ ) and representative horizontal intensity line scans. ....	64
Figure 49.	NSOM signals of a ZnO nanowires cluster with much smaller wires (20 $\mu\text{m}$ x 20 $\mu\text{m}$ ) and representative horizontal intensity line scans. The NSOM tip used is 150 nm in diameter.....	65
Figure 50.	Schematic diagram of the scanning area and beam-tip displacement. ....	66
Figure 51.	(a) AFM and (b) NSOM scans of a ZnO nanowire (2 $\mu\text{m}$ x 2 $\mu\text{m}$ ). The electron beam is approximately 0.5 $\mu\text{m}$ below the two pictures. .	66
Figure 52.	Intensity line scan (linear and semilogarithmic plots) of ZnO NSOM signal along the wire.....	67
Figure 53.	OM image of Si microtrench in SEM picture mode. The wires are in the intermediate regions between the 2 bright spots. ....	70
Figure 54.	HP sample CVD 895 at 10000X. ....	71

THIS PAGE INTENTIONALLY LEFT BLANK

## LIST OF TABLES

Table 1.	30 keV SEM beam width diameter dependence on probe current .....	24
Table 2.	Measured Diffusion length for wire 1 and 2 .....	47
Table 3.	Effect of <i>increasing</i> parameters. ....	55
Table 4.	HP Si nanowire samples. ....	70

THIS PAGE INTENTIONALLY LEFT BLANK

## ACKNOWLEDGMENTS

I would like to extend my sincere appreciation to my thesis advisor, Dr. Nancy M. Haegel, for her patience and dedication throughout every stage of the research including writing this thesis. From my first classes at NPS all the way until graduation, Dr Haegel has given me relentless support and intellectual guidance. Her support and advice extend beyond research work. My family and I felt indebted to her for her understanding and compassion. I would also like to thank my co-advisor, Prof Luscombe for his efforts in ensuring the quality of this thesis.

My appreciation extends to Dr Woong Kim of the Molecular Foundry, LBNL, for fabricating the ZnO wires that are so important for this work. I wish to thank Sam Barone for his efforts in helping in my experiments particularly in coupling optical fibers. Additionally, I thank Chanman Park for allowing me to use their high-powered optical microscope in the Mechanical Engineering Department. I'm grateful to Andrey Ignatov of Nanonics for our many discussions on the use of AFM/NSOM system. Finally, I would like to thank NovelX for using their first generation SEM for high resolution imaging. This work is supported by the National Science Foundation through Grant DMR-0526330.

To my son, Bing, and daughter, Shuen, whenever you come near my desk, you are taking away my stress while I'm at work. Finally and most importantly, I want to thank my wife, Chin Yen, for her unwavering patience and tremendous understanding while I spent countless nights working on this research. This is all dedicated to my wife, son, daughter and my expected third child.

THIS PAGE INTENTIONALLY LEFT BLANK

## I. INTRODUCTION

*Any intelligent fool can make things bigger, more complex, and more violent. It takes a touch of genius - and a lot of courage - to move in the opposite direction.*

*Anyone who has never made a mistake has never tried anything new.*

Albert Einstein

### A. BACKGROUND

Extensive research has been done on nanoscale structures. Starting with Richard Feynman, many recognized the potential applications in constructing nanoscale electronic and optoelectronic devices. Nanowires are attractive building blocks for these nanoscale devices. Current research focuses primarily on producing nanowires and characterizing their properties [1]-[5]. Current challenges include coupling the wires to existing semiconductor technologies for practical applications. There is a parallel need to develop characterization tools at this small scale in order to understand the novel physical properties of one-dimensional nanoscale materials.

In recent years, a new technique for characterizing minority carrier transport properties (diffusion and drift) has been developed [6]-[7]. Localized charge is generated by an electron beam and by capturing/observing the emission from recombination, the charge motion is imaged spatially by an optical microscope (OM). The electron beam is generated in a scanning electron microscope (SEM) and incident on a luminescent sample. The resulting intensity distribution allows for quantitative study of transport characteristics. This approach has been successfully demonstrated in 2-Dimensional heterostructures and with high quality materials. It is most easily applied when the luminescence is strong and the diffusion lengths are significantly greater than the generation spot size.

The work in this thesis begins the process to extend the transport imaging technique to nanowires. Due to the nanoscale size, there is a range of challenges to overcome. First, the OM is detecting light in the far field and its resolution is fundamentally diffraction limited. However, the dimensions of a nanowire are on the order of wavelength of light and hence reach the limits of the OM's resolving power. To overcome this, a near-field optical detector is used (near-field scanning optical microscope or NSOM). The NSOM operates on an atomic force microscope (AFM) platform and is installed internal to the SEM. The goal is to generate charge on a single wire and scan the NSOM tip to map the intensity distribution due to recombination along the wire. Special features on the Nanonics AFM/NSOM allow for such an experiment. Practically, the NSOM is not simple to operate and the biggest hurdle is the charging interaction of the scanning NSOM tip with the electron beam.

Another hurdle in transport imaging of nanowires is the size dependant properties of the wires. When sizes are small, surface recombination can completely overwhelm the band-edge emission of the wire. Quantization of energy levels restricts electron motion when the wire size is small enough for quantum effects to become significant. These complications need to be taken into account while conducting and interpreting transport imaging experiments. Finally, emission from single nanowire structures may be relatively weak. The luminescence from a single nanowire will be affected by surface recombination, in addition to having a very small emission area.

Despite the challenges, this thesis work demonstrated collection of emission from individual ZnO nanowires. With the OM at low resolution, a preliminary measurement of diffusion length is made. Operation of the AFM/NSOM inside the SEM was achieved and control measurements were performed. Finally, luminescence light is imaged from single ZnO nanowires, which shows promising results and provides direction for future work.

## **B. MILITARY RELEVANCE**

In recorded history, advances in technology almost always drive revolutions in military affairs (RMA). With the emergence of transistors in 1947, semiconductors and electronic devices have been instrumental in shaping military tactics, doctrines and even strategies. With the advances in optoelectronics, solar cells, high capacity integrated circuits (ICs) and laser electronics, the battlefield was revolutionized. Nano-technology is poised to be the next 'big thing' as its exploitation will directly influence the development of the next generation battlefield. For example, in the current RMA, there is a need for nano-devices in autonomous war fighters (land vehicles, undersea vehicles and aerial platforms).

Nanowires and quantum dots have tremendous potential in military applications. Nanoscale electronic components made from nanowires can be extended to conventional computer circuits, enhancing processing power and allowing higher density packing in existing systems. As a result, huge levels of investments are being made on nanotechnology by the military. One prominent example is the MIT Institute for Soldier Nanotechnologies [8]. Another is the wide range of The Defense Advanced Research Projects Agency (DARPA) initiations in nanotechnology.

The work in this thesis seeks to develop a new technique to characterize the physics of electrical carrier transport and quantum properties of nanowires.

## **C. THESIS OVERVIEW**

Chapter II provides the theoretical background of transport imaging. This chapter includes the theory of luminescence from semiconductors and provides a brief description of nanostructures and nanowires. This section includes mathematical modeling of minority carrier transport in a nanowire.

Chapter III describes the experimental approach. Several specialized pieces of equipment are used in this thesis work and the chapter gives a brief description of the challenges that are posed by this unique instrumentation. Part of the chapter describes the limitations of SEM-OM and reviews the diffraction-limited resolution of a microscope. There is also a short description of the data extraction and analysis methods used.

In Chapter IV, the first results of imaging the wires are reported. The data extraction and modeling are also presented. Noting that the resolution has reached its limits using SEM-OM, Chapter V presents the exploratory experiments using the SEM-AFM/NSOM. In this chapter, the successful operation of AFM/NSOM within the SEM is demonstrated. In addition, calibration and system resolution are explored. Chapter VI presents the first NSOM image of ZnO nanowires. Chapter VII shows the results of imaging silicon nanowires.

Finally, Chapter VIII summarizes the conclusions and provides suggestions for future work.

## II. TRANSPORT IMAGING OF NANOWIRES - THEORY

### A. TRANSPORT THEORY

#### 1. Luminescence Phenomena

Luminescence in semiconductors is the process of photon emission when a certain form of non-thermal energy is provided to the sample. The excess energy can excite electrons from the valence band to the conduction band, creating electron hole pairs. The resultant emission is due to an electronic transition between an initial state  $E_i$  and the final state  $E_f$ , also referred to as recombination. The energy or the wavelength of the emitted photon can be found from the relation

$$E_f - E_i = h\nu = \frac{hc}{\lambda}$$

Using light as the energy source (photons), the phenomenon is called photoluminescence (PL). When electrons are used for excitation, it is known as cathodoluminescence (CL). In CL, external energy is incident using an electron beam such as from an SEM, creating electron-hole pairs in the semiconductor. By the process of its recombination, light is emitted (Figure 1).

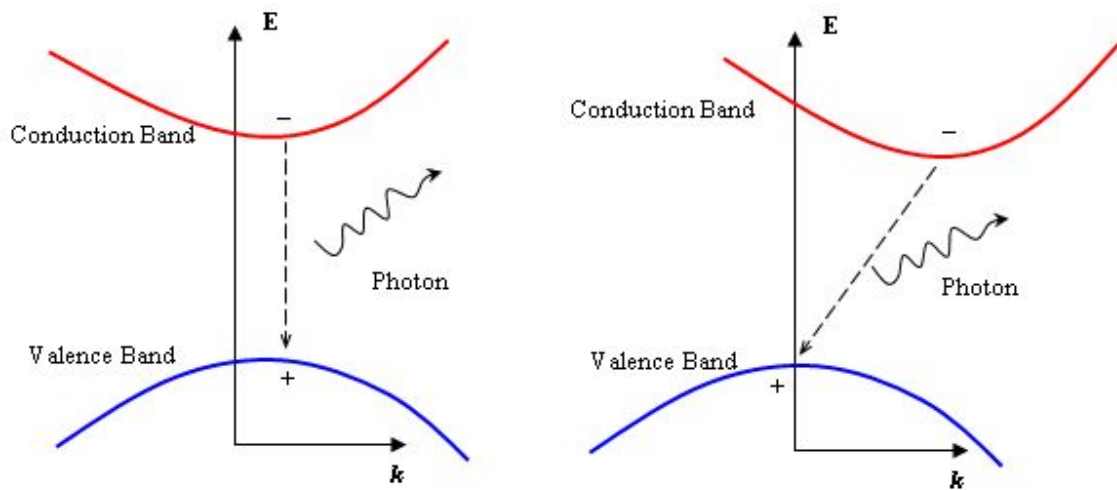


Figure 1. Band diagrams of (left) direct band gap, (right) indirect band gap materials

In direct band gap materials, transitions from the bottom of the conduction band to the top of the valence band are vertical in momentum space. Therefore radiative recombination of the electron-hole pairs is relatively likely. Since energy and momentum must be conserved, band to band recombination in indirect bandgap materials requires participation of phonons. The recombination must include emission of a photon and a phonon, a lattice vibration. Due to emission of this extra particle, the probability of such a process is significantly lower than that of direct transitions. Therefore, emissions from indirect bandgap (e.g., silicon) materials are relatively weak.

The type of the radiative transition just discussed is an intrinsic or band-to-band luminescence. One can also identify luminescence from other forms of recombination such as extrinsic and exciton luminescence. Extrinsic or impurity luminescence originates from the radiative recombination of free electrons to donors or free holes to acceptors.

Luminescence is an efficient tool to study the excited electronic states in solids. Since the luminescence intensity is determined both by the population of the excited states and the optical-transition probabilities, luminescence offers an advantage in analyzing the fine structure of excited states.

## 2. Cathodoluminescence

Cathodoluminescence occurs when a high energy (~2 to 40 keV) electron beam impinges onto a semiconductor and results in the promotion of electrons from the valence band into the conduction band. Luminescence is produced when these electron-hole pairs recombine. The characteristics of light emitted depend on properties of the material, its purity and defect distribution. Compared to PL, one 20 keV electron can generate thousands of electron-hole pairs, whereas a photon in a PL process generates only one electron-hole pairs. Also, since the incident beam energy is large, CL is easily generated in both wide bandgap and narrow bandgap materials. Hence CL offers a good tool for investigating properties of a wide range of semiconductors.

When an electron beam hits a semiconductor, the number of electron-hole pairs generated for each incident beam electron is given by

$$G = \frac{E_b(1-\gamma)}{E_i}$$

where  $E_b$  is the electron beam energy,  $E_i$  is the average energy required to generate an electron-hole pair which is related to material band gap, and  $\gamma$  is the fractional energy loss due to the backscattered electrons [9]. For non-relativistic energies (less than 50 keV), the (Gruen) range of the electron penetration which depends on the electron beam  $E_b$  is approximated by

$$R_e = \left( \frac{k}{\rho} \right) E_b^\alpha$$

where  $k$  and  $\alpha$  are parameters dependent on the beam energy and atomic number of the material and on energy, and  $\rho$  is the density of the material. According to Kanaya and Okayama [10], the penetration range can be approximated as

$$R_e = \left( \frac{0.0276A}{\rho Z^{0.889}} \right) E_b^{1.67} (\mu m)$$

where  $E_b$  is in keV,  $A$  is the atomic weight in g/mol,  $\rho$  is in g/cm<sup>3</sup> and  $Z$  is the atomic number. Figure 2 shows the electron range as a function of electron beam energy for 3 common semiconductors.

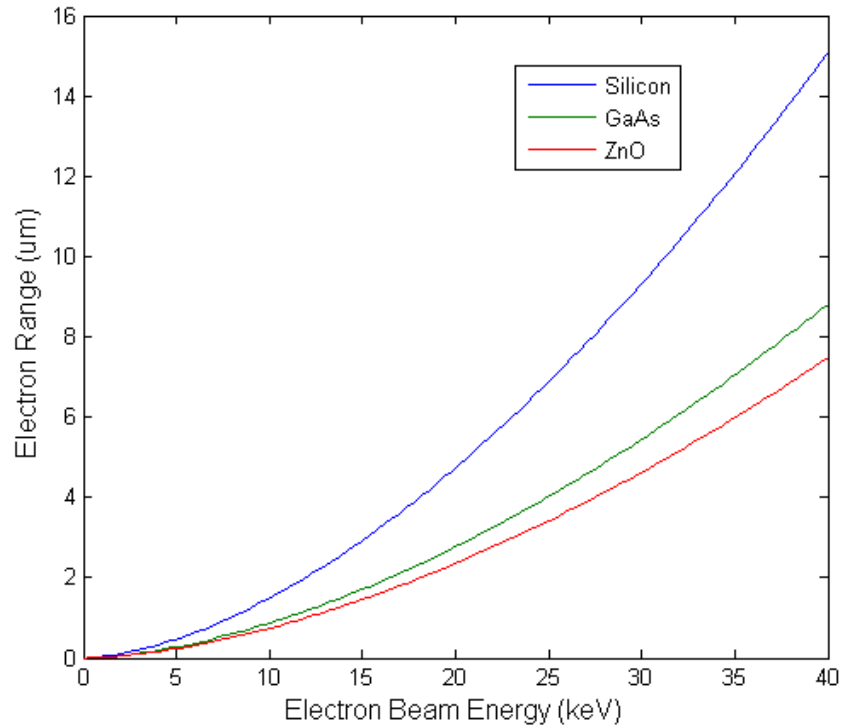


Figure 2. Electron range vs electron beam energy for Si, GaAs and ZnO.

A universal depth dose function (proposed by Everhart and Hoff [12]) can be used to relate the penetration range  $R_e$  for a given beam energy with the

penetration depth. This function represents the number of electron-hole pairs generated per electron per unit depth per unit time. The dose function can be written in terms of normalized depth

$$g(z) = 0.6 + 6.21\left(\frac{z}{R_e}\right) - 12.4\left(\frac{z}{R_e}\right)^2 + 5.69\left(\frac{z}{R_e}\right)^3$$

To illustrate graphically, the depth-dose function for ZnO is plotted in Figure 3.

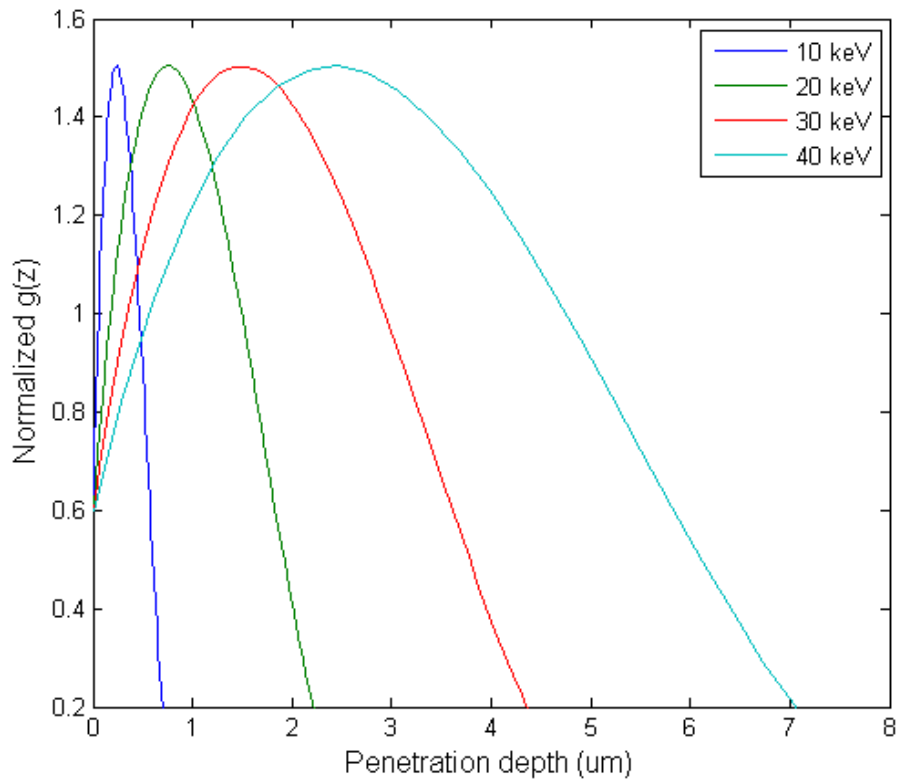


Figure 3. Penetration depths, according to the depth-dose function for ZnO at various beam energies.

Note that for nano-structures, the penetration depth is far beyond the physical dimension – i.e., for a nanowire sample of about 100 nm in diameter, a normal SEM beam of 20 keV will penetrate far beyond the wire into its substrate and hence create complications in CL analysis (Figure 4). Furthermore, the

types of distribution approximation at the charge generation region also affect the shape of the generation volume. The commonly used approximations are the point source, the uniform sphere and the Gaussian distribution functions. The Gaussian model shows a better fit to the experimentally determined pear-shaped distribution [9].

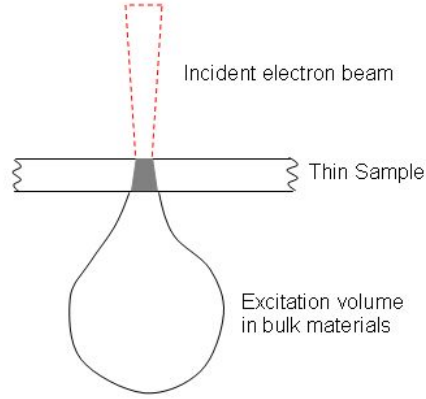


Figure 4. Pear shape excitation volume in bulk samples

The overall CL intensity can be derived from solutions to the continuity equation, using a point source approximation. It can be shown that for electron generation  $G$  with beam current of  $I_b$ , the CL intensity is

$$L_{CL} = f_D f_A f_R \eta \left( \frac{G I_b}{e} \right)$$

where  $f_D$ ,  $f_A$  and  $f_R$  are factors that account for detector efficiency, absorption and internal losses respectively. The detector efficiency takes into account the light collector loss, transmission loss of the monochromator and quantum efficiency of photomultiplier.  $\eta$  is the radiative recombination efficiency ( $\eta = \frac{\tau}{\tau_{rr}}$ )

[9]. Here, we see that CL intensity is proportional to generated carrier concentration,  $L_{CL} \sim \frac{n}{\tau_{rr}}$ .

### 3. Carrier Transport

Relevant transport processes of generated carriers include drift, diffusion, thermionic emission, tunneling, and impact ionization. If a semiconductor is under the influence of a carrier (electron or hole) concentration gradient or an electric field, there will be motion of these charge carriers. Drift and diffusion properties are most directly relevant to this characterization approach [11].

Under an applied electric field, each electron will experience a force  $-qE$  and be accelerated along the field (in the opposite direction) during the time between collisions. This force gives rise to an added velocity of the electron from its thermal velocity. Therefore, this field-dependent velocity is called the drift velocity [13]. By conservation of momentum, the momentum applied to the electron equates to the momentum gained. Hence we write,

$$qE\tau_c = m_n v_n$$

The drift velocity  $v_n$  is then,

$$v_n = \left( q \frac{\tau_c}{m_n} \right) E, \quad \text{or} \quad v_n = \mu E$$

The equation states that drift velocity is proportional to  $E$  and that the proportionality factor is called the electron mobility  $\mu$ , where  $\mu = q \frac{\tau_c}{m_n}$ . Mobility describes how strongly the motion of electrons in the lattice is affected by an applied field and thus is an important semiconductor parameter.

Consider another scenario where instead of an applied electric field, there exists a spatial variation in carrier concentration. The carriers tend to move from higher concentration region to a lower concentration region. This motion is referred to as diffusion and the associated current, in the case of electrons, can be written as

$$J_n = -qv_{th}l \frac{dn}{dx}$$

where  $v_{th}l = D_n$  is the diffusion coefficient (or diffusivity),  $l$  is the mean free path and  $v_{th}$  is thermal velocity. The diffusion current is proportional to the spatial derivative of electron density. The above equation says that for negative concentration gradient (that is, electron density decreases with  $x$ ), electrons will 'diffuse' toward the positive  $x$ -direction.

Mobility and diffusivity are two important constants that characterize carrier transport properties of a semiconductor. The Einstein relation relates  $D$  and  $\mu$  together for useful applications. From earlier equations,  $\tau_c = \frac{\mu m_n}{q}$ , and

the relation  $l = v_{th}\tau_c$ , we obtain 
$$D_n = v_{th}^2 \left( \frac{\mu m}{q} \right)$$

By conservation of energy, 
$$\frac{1}{2}mv^2 = \frac{1}{2}kT,$$

yields 
$$v_{th}^2 = \frac{kT}{m}$$

therefore 
$$D_n = \left( \frac{kT}{m} \right) \left( \frac{\mu m}{q} \right), \text{ or } D_n = \left( \frac{kT}{q} \right) \mu_n$$

The Einstein relation also applies to  $D_p$  and  $\mu_p$  – parameters for holes. Experimentally, the diffusion distance  $L$  can be measured easily using transport imaging techniques. With the relationship of  $L = \sqrt{D\tau}$ , where  $\tau$  is the minority carrier life time, material constants  $D$  and subsequently  $\mu$  can be obtained.

#### **4. Transport Imaging**

Direct transport imaging techniques used in this thesis provide a means to experimentally obtain the  $\mu\tau$  product and the minority carrier diffusion length  $L$ , in a single, non-destructive measurement. Consider an incident electron beam interacting with a sample surface; it generates electron-hole pairs in a small region. This creates a minority concentration gradient and hence diffusion of carriers occurs (and drift if  $E$  is applied). In steady-state, the density of minority carriers will be distributed spatially due to drift, diffusion or interaction volume. When minority carriers recombine, light is emitted and its intensity is directly proportional to minority carrier density, assuming a larger majority carrier population. By capturing a spatial image of the luminescence, and from the characteristics of the distribution, one can obtain  $\mu\tau$  and  $L$ . It is this direct observation of the spatial distribution that causes the approach to be significantly different than standard CL.

### **B. NANOSTRUCTURES AND NANOWIRES**

The term nanowires refer to wires that have dimensions in 2 of 3 dimensions on nanometer scales. The term is also used to describe carbon crystalline tubes – carbon sheets that wrap around a conducting medium. For this thesis, we are working only on the inorganic semiconductor type. The potential applications for nanowires are intriguing but there exist fundamental challenges both in fabrication and characterization at the nanometer scale. Transport behavior of macro-level semiconductors is well understood, but in the nano regime, fundamental studies are required.

#### **1. Nanowire Applications**

Current and potential applications of nanowires are very broad. To date, nanowires have been used as components of electronics, optics, mechanics, and

sensing technology. Moreover, nanowires are used in a host of diversified fields including assembling biological species [14] and using nanowire sensors for medical diagnostics [15].

Semiconductor oxides have been the focus of recent research because the IT industry is approaching fundamental limits of CMOS technologies [16]. The key problem is the interconnection of the wires to any electronic entity. Once this constrain is solved, conducting wires offer the possibility of connecting molecular-scale devices in a molecular computer. Apart from being just a 'wire' and only smaller, if a nanowire semiconductor can be successfully built as a p-n junction – the basic building block of modern electronics, the impact it can make to the world is tremendous.

Another application of nanowires is using them for laser devices and LEDs. A team from University of California San Diego (UCSD) and Peking University (Beijing, China) claimed that zinc oxide nanowires may yield cheaper LEDs and solar cells [17] than the currently used semiconductor materials.

Special properties of a nanowire can also be exploited. One recent example is the use of  $\text{KNbO}_3$  nanowires for scanning light microscopy [18]. According to Peidong Yang and his team from UC Berkeley, LBNL and Sony, the nonlinear crystal polarization phenomenon inside the wire enables production of ideal sources of tunable coherent light for subwavelength microscopy.

## **2. Fabrication of Nanowires**

Nanowires do not exist in nature and hence have to be artificially produced. There are major efforts among both commercial and research institutions to evaluate many different methods to produce nanowires. In this thesis work, there are three types of differently prepared samples.

The ZnO samples that are used extensively in the thesis were grown by vapor-phase transport using metal catalysts. In this method a vapor-liquid-solid

(VLS) mechanism is used. Gold (Au) is used as a catalyst. An Au thin film is heated and deposited on a silicon substrate. An equal amount of solid ZnO powder and graphite are heated at high temperature under a constant flow of argon. The ZnO powder is reduced to Zn and CO/H<sub>2</sub>O vapor. At a lower temperature downstream, the Au particles on the silicon substrate served as nucleation sites for the condensation of zinc (Zn) vapor [1]. With the CO/H<sub>2</sub>O vapor as the oxygen source, ZnO nanowires grow on the Au clusters.

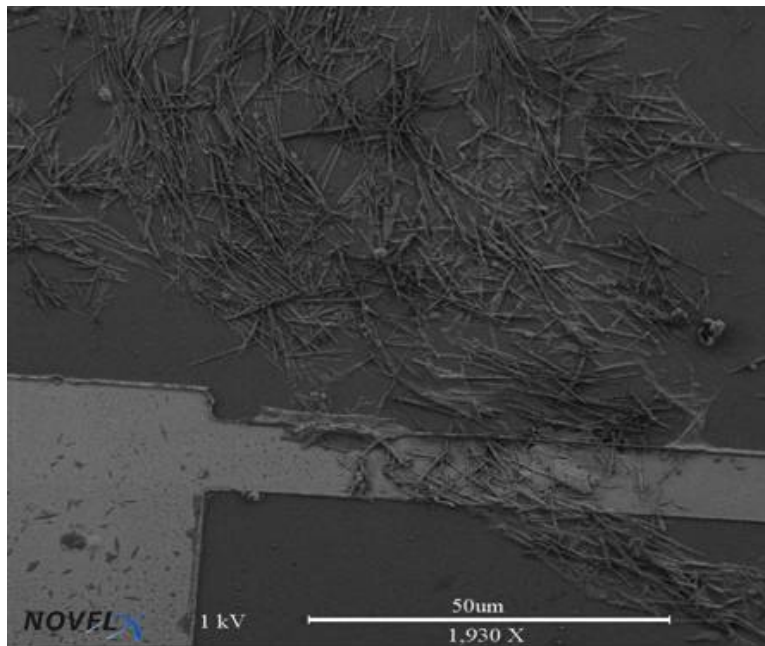


Figure 5. Cluster of nanowires produced by VLS mechanism (sample A).

The resultant nanowires are on the order of 80-120 nm in diameter and up to 20  $\mu\text{m}$  long [1]. A collection of ZnO wires on a Si substrate is shown in Figure 5. Size control of the wires is achieved by varying the thickness of the Au thin film. The idea is based on a possible direct correlation between the size of the catalytic particles and the resulting diameters of nanowires. Metal contacts with 2

- 20  $\mu\text{m}$  gaps are then deposited onto the wires. By careful alignment, a single wire can be designed to bridge across the gap, and a nanowire device is produced (Figure 6).

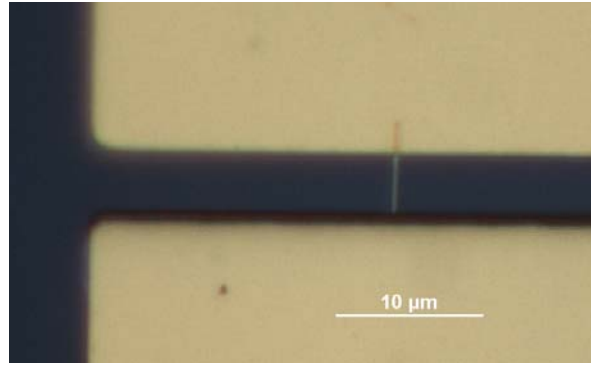


Figure 6. Optical image of a ZnO wire across a 5  $\mu\text{m}$  gap (sample B).

In the thesis work, we have also investigated a set of Si nanowires which were prepared somewhat differently from Sample A, although a VLS process is still used. This top down process combined the techniques of microfabrication using photolithography for trenches and wire growth on catalyst sites. The basic idea is that the trenches are carefully etched such that a Si (111) surface is exposed on the side walls of the trench. Then by the VLS mechanism on Au catalysts, the wires are grown laterally until they bridge to the other Si (111) surface [2]. Figure 7 shows a schematic illustration of the top down process. These wires are usually suspended above the  $\text{SiO}_2/\text{Si}$  substrate.

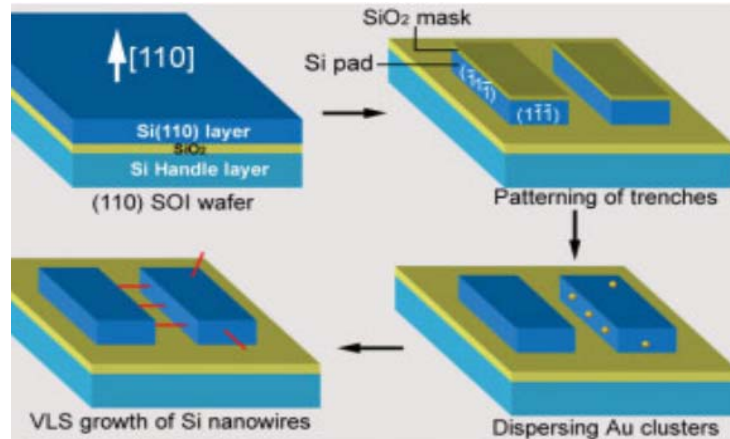


Figure 7. Schematic illustration of bridged nanowire fabrication (from [2]).

Figure 8 shows an SEM picture of Si 'top-down' wires suspended across the sides of a trench 2  $\mu\text{m}$  wide. Over time, impurities can accumulate on the nanowires, which is quite apparent in Figure 8, which shows the wires almost one year after storage in room air.



Figure 8. Si wires bridging the trenches.

The third type of wires were fabricated at Hewlett Packard (HP) laboratories. These are Si wires grown by a chemical vapor disposition (CVD) process [3]. This process differs from VLS mechanism as the wires are nucleated from Ti containing islands. The Ti islands are formed by introducing Ti containing gas onto the Si substrates at high disposition temperatures. After the islands are formed, a lower disposition temperature for the Si disposition is used with injection of Si containing gases. Si wires are then nucleated from these Ti islands. Figure 9 shows the SEM images of several CVD grown samples.

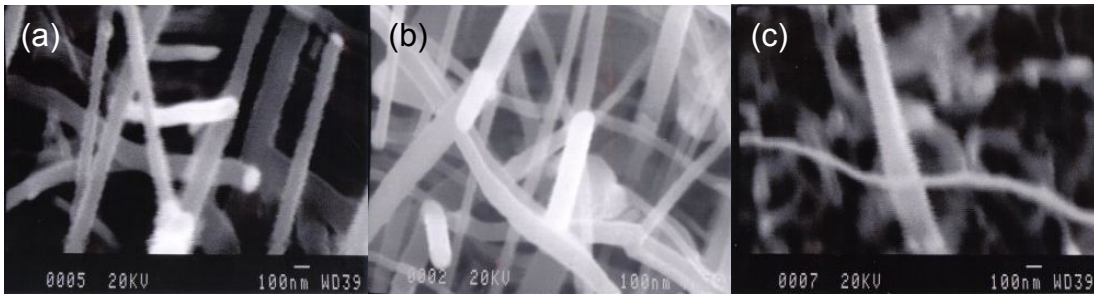


Figure 9. HP nanowires at 50000X. (a) CVD 893, (b) CVD 895, (c) CVD 904.

### 3. Properties of Nanowires

Intuitively, the electrical properties such as conductivity of a nanowire are expected to be different from the corresponding bulk material. This is true, for example, if we consider the size (diameter) of the wire below the electron mean path of the bulk material, where scattering from the wire boundaries becomes a significant effect (see Chapter IV - A2), and reduces conductivity.

In addition, the energy levels of electrons going through a metal wire at nano-scale can assume discrete values. The discrete level are believed to be in multiples of the von Klitzing constant [19],

$$G = \frac{2e^2}{h}$$

where  $e$  is the electron charge and  $h$  is Planck's constant. Each quantized energy level allows transport of electrons. The smaller the dimension of the wire, the less of these discrete levels and hence less transport. Put simply, conductivity of the wire is significantly reduced. In semiconductor wires like Si, GaAs or ZnO, the effect of reduced conductance is even more pronounced because of the lower electron density and lower effective mass [5], [20].

Figure 9 shows spacing between energy states (e.g., in the conduction band) of ZnO, GaAs and Si as a function of size. Assuming the sides of the wire as an infinite quantum well confining 2 of 3 dimensions of the material. The energy between states is

$$\Delta E = (n_2 - n_1)^2 \frac{\hbar^2 \pi^2}{2m^* L^2}$$

where  $m^*$  is the electron effective mass of the semiconductor,  $L$  is width of quantum well (i.e. diameter of wire) and  $\hbar$  is Planck's constant scaled with  $\frac{1}{2\pi}$ .

The difference in energy between states becomes very significant in the region below 30 nm to 50 nm dimensions. Discrete quantum mechanical effects are bound to affect the wire's properties below 30 to 50 nm diameter. In this work, the nanowires are in the realm of 50 to 200 nm, so quantum effects are expected to be negligible.

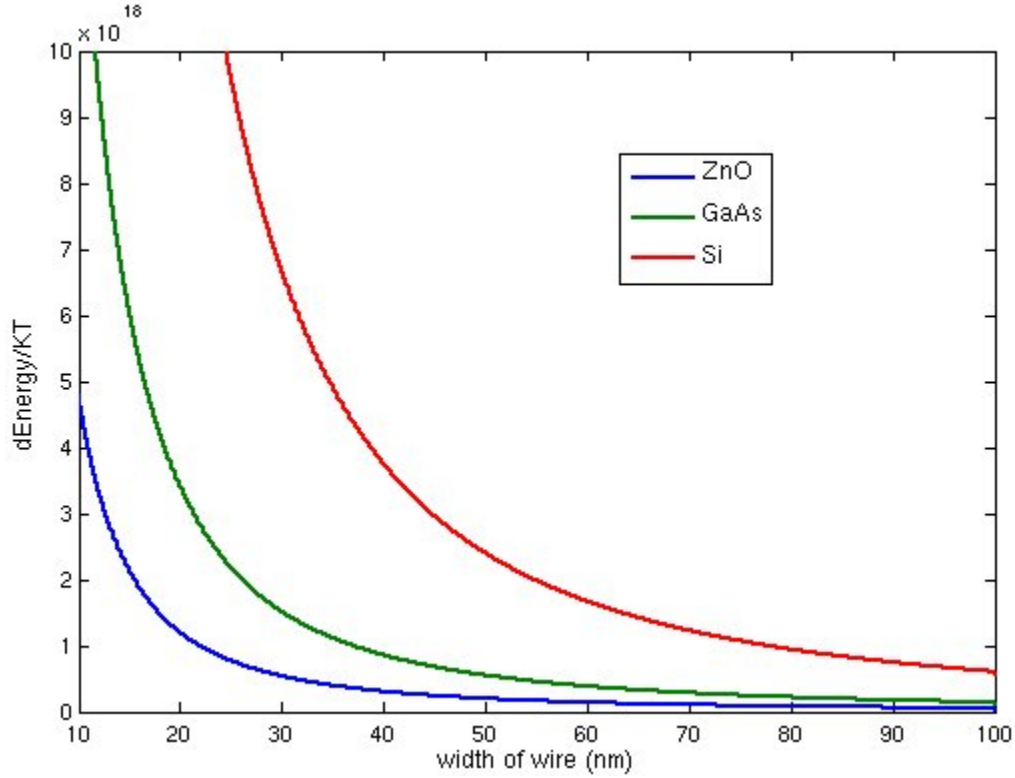


Figure 10. Energy between states/kT (Energy of  $n=2$  to  $n=1$ ) of ZnO, GaAs and Si as a function of quantum well width (aka diameter of nanowires) for  $T=300K$ .

In summary, these quasi-one-dimensional (quasi-1D) structures have unique properties unattainable in bulk due to both surface and potentially quantized state effects. This presents an added difficulty in characterizing nanowires experimentally compared with their bulk counterparts.

### C. MODELING TRANSPORT IN THE ONE DIMENSIONAL LIMIT

The nanowires described in previous sections vary from 50 to 200 nm diameter, a couple orders of magnitude smaller than their length ( $\sim 5$  to  $10 \mu m$ ). This qualifies them as quasi-1D structures and hence a 1D transport model of diffusion and drift is required for the recombination modeling of these wires. If the charge generation is an ideal point source, the intensity distribution [6]-[7] is

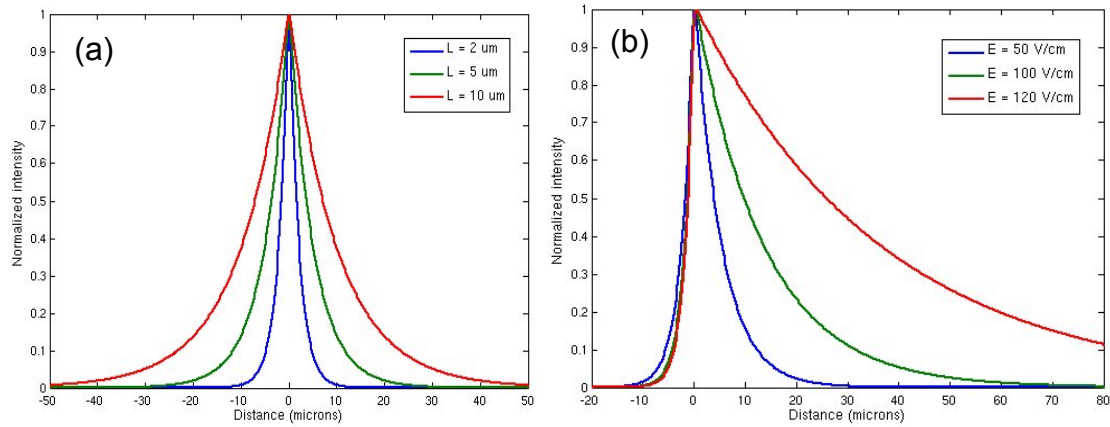
$$I \approx e^{-\frac{x}{L}}$$

Practically, an SEM electron beam generates the charge and the beam has a finite beam width, as opposed to an ideal point source. Assuming the generation region has a Gaussian distribution, a 1D steady state model of intensity distribution has been previously developed [21]. The integral equation in it's simplest form is

$$I_{SS} = C \int_{-\infty}^{\infty} e^{-\left[ m\xi^2 - \frac{S(x-\xi)}{2L^2} + \frac{|x-\xi|\sqrt{S^2+4L^2}}{2L^2} \right]} d\xi$$

where  $x$  is distance from the center of generation region,  $m$  is a parameter inversely proportional to size of generating region,  $S$  is the drift length in the presence of an applied  $E$  field ( $S = \mu\tau E$ ) and  $C$  is a prefactor constant containing diffusion/drift lengths ( $L$  and  $S$ ) and the size of Gaussian generation region,  $m$

( $C = \frac{g}{2\sqrt{S^2+4L^2}} \sqrt{\frac{m}{\pi}}$ ). Figure 11a, 11b and 11c show the normalized intensity distribution of varying  $L$ ,  $m$  and  $E$  with the model. Figure 11d shows the close up plot of the peak for Figure 11c.



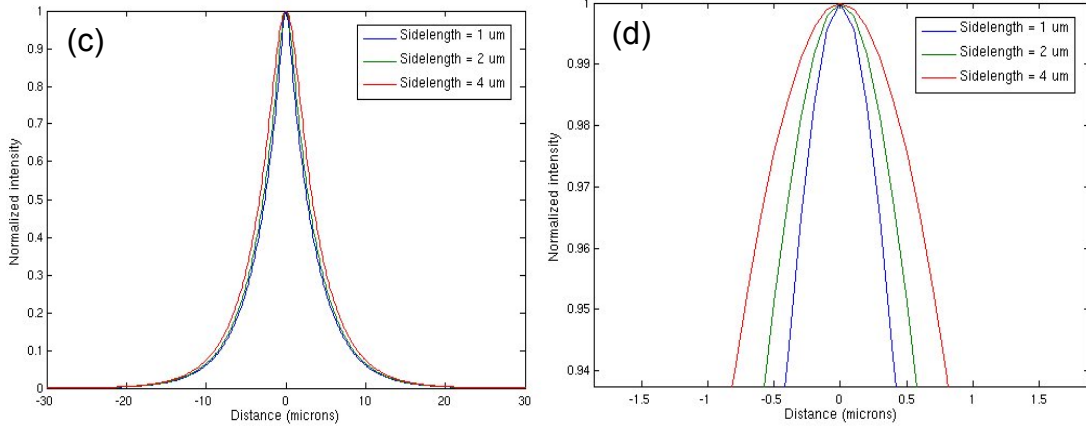


Figure 11. Numerical calculations of the steady state model: (a) Normalized intensity as a function of  $L$ ,  $m=8$ ,  $E=0$ . (b) Normalized intensity as a function of  $E$ ,  $m=8$ ,  $L=3.5 \mu\text{m}$ . (c) Normalized intensity as a function of sidelength,  $L=3.5 \mu\text{m}$ ,  $E=0$ . (d) Expansion plot of (c).

Figure 11a shows the intensity distribution for fixed  $E$  and  $m$ , for different values of  $L$ . Figure 10b shows the intensity distribution for a fixed  $m$  and  $L$ , when different value of  $E$  is applied. For Figure 11c and 11d, side-length is used to represent generation region (side-length is the lateral length of a generation region and is equal to  $\sqrt{\frac{8}{m}}$ ). As the generating region gets smaller, the peak at  $x = 0$  becomes sharper, approaching a point source generation.

The 2D model has been previously used to analyze experiment results for transport in 2D heterostructures and have found to describe the luminescence distribution, both with and without applied electric field. In the absence of quantum effects due to lower dimensionality discussed in previous sections (i.e. for wires  $> 50 \text{ nm}$  in diameter), the 1D model is expected to predict the intensities distribution for quasi-1D structures.

### III. EXPERIMENTAL TECHNIQUES

#### A. THE SCANNING ELECTRON MICROSCOPE (SEM)

The SEM used for this thesis work is a JEOL 840A SEM. This provided a platform for the source of electrons in CL. The light emitted from the recombination process can be collected by either a parabolic mirror and spectrometer or an optical microscope (OM) system which are both connected to the SEM chamber (Figure 12). The SEM chamber is an evacuated environment with a cold stage for variable temperature experiments. The cold stage allows continuous liquid helium flow, so experiments can be performed at temperatures as low as 4.2 K.

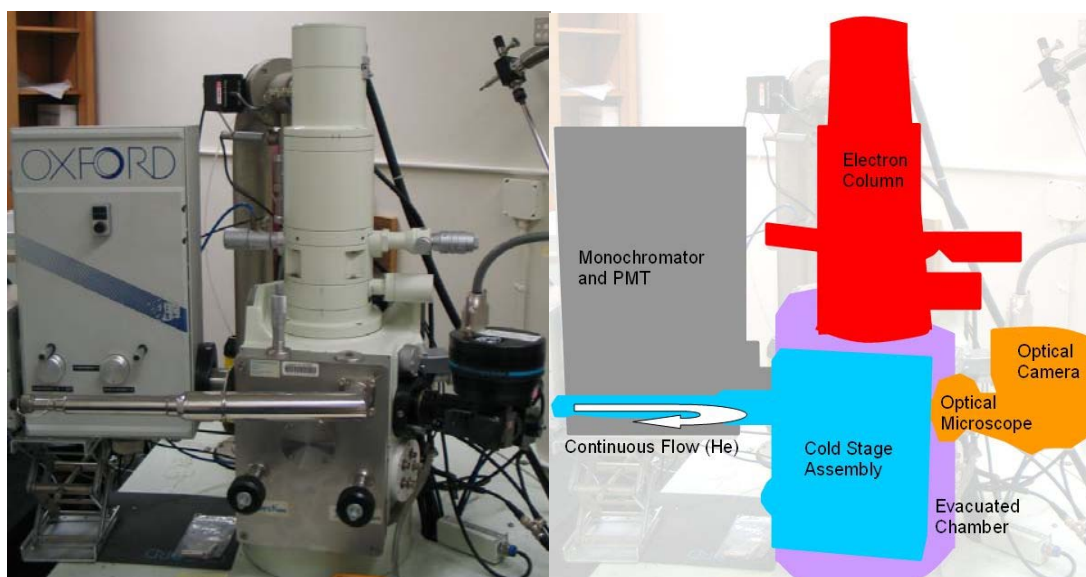


Figure 12. OM and spectrometer connected to JEOL 840A SEM.

In the SEM, electrons are thermionically emitted from a tungsten filament. The electrons are focused into a beam with a very fine focal spot. The size of the spot can be controlled by varying the probe current. The spot size is particularly

important because of the finite width of the nanowires, which is on the order of tens of nanometers. Table 1 summarizes measured surface spot sizes in our SEM as a function of probe current.

Probe Current (A)	16%-84% ( $2\sigma$ ) (nm)	FWHM (nm)
$1 \times 10^{-11}$	34	40
$3 \times 10^{-11}$	39	46
$1 \times 10^{-10}$	48	56
$3 \times 10^{-10}$	107	126
$1 \times 10^{-9}$	139	163

Table 1. 30 keV SEM beam width diameter dependence on probe current

The electron beam passes through pairs of scanning coils in the objective lens, which deflect the beam horizontally and vertically so that it scans in a raster fashion over a rectangular area of the sample surface. When the primary electron beam interacts with the sample, the electrons lose energy by repeated scattering and absorption within a teardrop-shaped volume of the specimen known as the interaction volume, which extends from tens of nanometers to many microns [9] into the surface depending on beam energy (eV) and the material. This volume size also determines the spatial and spectral resolution of conventional CL measurements. The energy exchange between the electron beam and the sample results in the emission of electrons and electromagnetic radiation. These can be detected to produce both topography (SEM) and luminescent images. Figure 13 shows an SEM image of a collection of ZnO nanowires. The SEM beam is scanned over a  $10 \mu\text{m} \times 8 \mu\text{m}$  region (11000X).

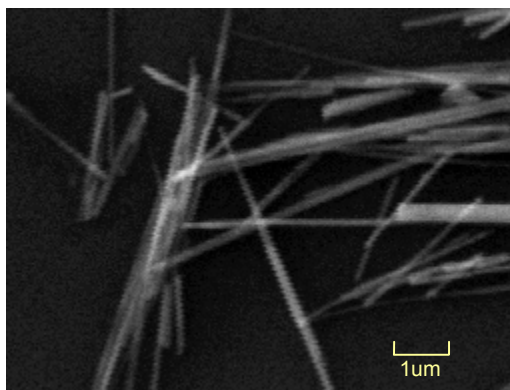


Figure 13. 'Picture' mode micrograph of ZnO nanowires on Si substrate (sample 'D') at working distance of 9 mm,  $6 \times 10^{-11}$  A , 20 keV, 11000X.

## 1. The Cathodoluminescence System

In this thesis, most optical experiments use the 'spot' mode of SEM operation, that is the electron beam is held fixed over a specific point on the sample. There will not be any topography images. Instead the CL system or a photodetector array is used to detect the photon emission from the electron-sample interaction. A Gatan (formally Oxford Instruments) CL system is connected to the SEM's internal chamber with a retractable arm. At the end of the arm is a parabolic mirror that guides the signal into the monochromator and then to a thermo-electrically cooled (TEC) GaAs Photomultiplier (PMT).

The CL system is used to study the spectroscopy of the nanowire luminescence. The spectrum of a nanowire emission allows us to separate the spectral characteristics of nanowires and their substrates. In this conventional CL system, the luminescence from a specific region on a sample can be resolved 'pseudo' spatially by reconstructing the luminescence intensities at each point to give a 2D 'picture' of relative intensities. This however assumes that at a given time of photon collection, all the photons are emitted from the point where the electron-hole pairs are generated by the electron beam. In transport carrier studies, the actual spatial distribution of photons emitted due to carrier diffusion

or drift is the goal. Conventional CL does not retain this spatial information and the actual distribution of luminescence due to transport is lost.

## 2. Optical Microscope and CCD Camera

To maintain the spatial information of the recombination, an optical microscope (OM) with a retracting arm connected to the SEM is used. A cooled Si CCD array camera (by Apogee Instruments) is used in passive detection mode at the other end of the OM. Figure 14 shows an example of how the spatial information is retained. The images show motion of charge in a GaAs/AlGaAs heterostructure under an applied AC field between two parallel plate contacts.

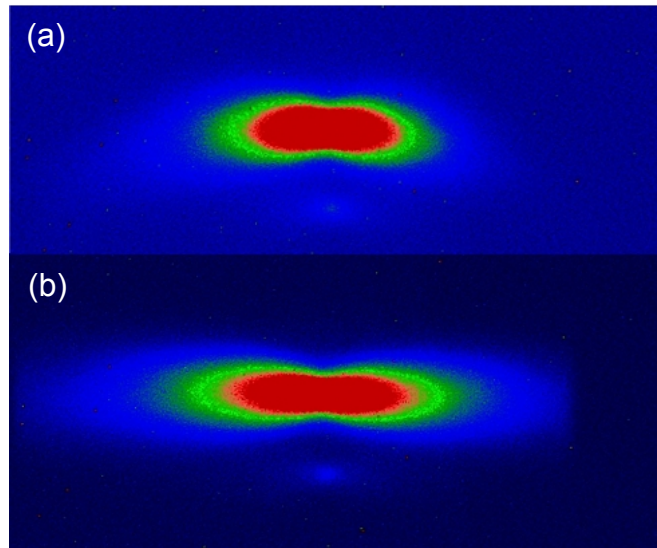


Figure 14. AC transport imaging (a) toward the fringe field (b) and in the center region of the parallel plate geometry. Each image is 330 (w)  $\mu\text{m}$  x 250 (h)  $\mu\text{m}$ . Electron-beam was  $3 \times 10^{-8}$  A and 20 keV (from [22]).

The Si CCD has a 2184 x 1472 pixel array and a physical pixel size of 6.8  $\mu\text{m}$  x 6.8  $\mu\text{m}$ . Since it is silicon based, only photon wavelengths of 350 nm to 1.1  $\mu\text{m}$  can be detected. The OM objective is a basic 2 lens system custom built with a reflecting mirror at the end of the arm with a hole to allow for passage of the

SEM electron beam. It has an objective magnification of  $\sim 20\times$ . A  $10\text{ }\mu\text{m} \times 10\text{ }\mu\text{m}$  scan on the sample hence will produce a  $200\text{ }\mu\text{m} \times 200\text{ }\mu\text{m}$  area on the CCD. Intuitively, this means that the system resolution is  $6.8/20 = 0.34\text{ }\mu\text{m/ pixel}$ . Practically, the CCD resolution has been measured to be  $\sim 0.4\text{ }\mu\text{m/ pixel}$ .

As with any microscopy, the optical resolution limit is an important consideration. The relationship for estimating the optical resolution of an incoherent emission [23] is

$$R \approx \frac{0.61\lambda}{NA}$$

where  $\lambda$  is the wavelength in  $\mu\text{m}$  and NA is the numerical aperture of the OM system. Figure 15 shows R as a function of the wavelength of interest for visible and near infrared (IR) emission.

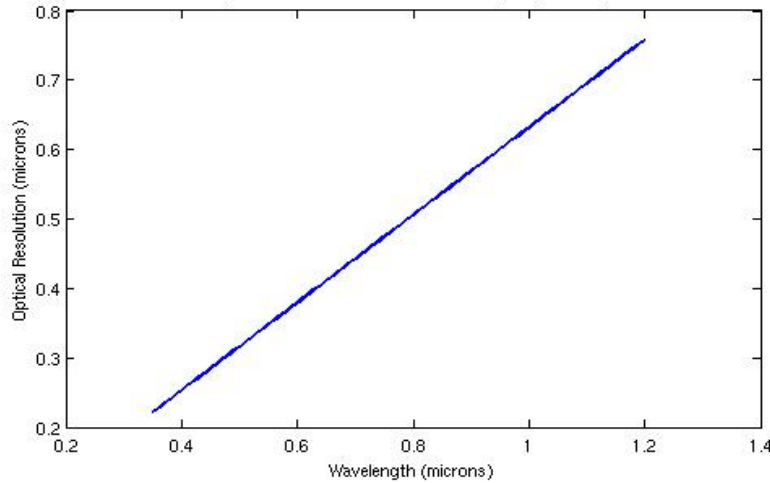


Figure 15. Optical resolution at different wavelength with NA = 0.95.

The optical resolution limits for the OM system therefore are in the range of 0.2 to  $0.7\text{ }\mu\text{m}$  over the wavelength range of interest. This means that, even with a higher magnification optical microscope, the system would be limited by diffraction for red to near IR emission. With the absence of specialized techniques (such as the Nonlinear stimulated emission depletion or STED [24]),

this optical resolution limit is the fundamental physical limit to the resolution of luminescence imaging – more commonly known as the diffraction limit.

### 3. The Diffraction Limit

In cathodoluminescence, we can consider that light emitted from the sample is made up of an array of incoherent point sources. When the point sources are incoherent, the lens system will form an image of the object that consists of a distribution of partially overlapping, yet independent Airy patterns. This pattern is the result of Fraunhofer diffraction, an equivalent effect through a circular aperture. Assume a light plane wave impinges on a screen containing a circular aperture and the resultant far-field diffraction pattern is spread across a distant observation screen. Using a focusing lens in-between, we can bring the observation screen in closer to the aperture without changing the diffraction pattern. If the lens is brought closer to the aperture and completely fills the aperture, the pattern is essentially unaltered. This shows that in any optical system - eye, telescope, microscope or camera lens – the Airy pattern is bound to occur [25]. Figure 16 shows a simulated Airy pattern.

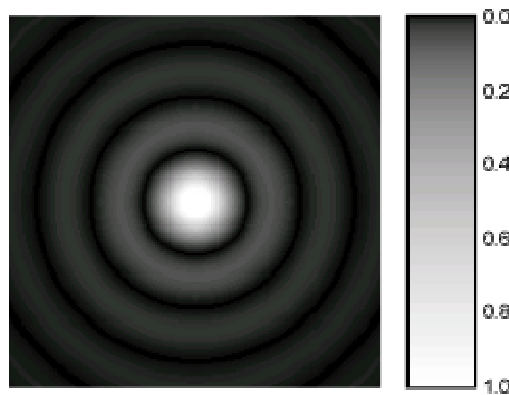


Figure 16. A simulated Airy pattern (normalized arbitrary units) (from [26]).

This Airy pattern represents the irradiance on the observation screen. The irradiance can be shown to obey the relationship,

$$I = I_0 \left( \frac{2J_1(\gamma)}{\gamma} \right)^2, \text{ where } \gamma \equiv \frac{1}{2} kD \sin \theta$$

where  $D$  is the diameter of the aperture and  $\theta$  is the angular radius of the Airy disc. The irradiance is a maximum at the center of the disc and has its first zero at  $\gamma = \frac{1}{2} kD \sin \theta = 3.832$  or  $D \sin \theta = 1.22\lambda$ . To simplify matters somewhat, we consider two equal-irradiance, incoherent distant sources. The image of each source occupies essentially the region of the Airy disc. Rayleigh's criterion for just resolvable images requires that the separation of the centers of the image is not less than the angular radius of the Airy disc. Thus for the limit of resolution, one finds

$$\Delta\theta_{\min} = \frac{1.22\lambda}{D}$$

where  $D$  is now the diameter of the lens in an optical system. This is illustrated in Figure 17a. If the lens is the objective of our optical microscope, the problem of resolving nanoscale objects is the same. The minimum separation,  $x_{\min}$ , of the two source objects near the focal plane of the lens is then given by

$$x_{\min} = f \Delta\theta_{\min} = f \left( \frac{1.22\lambda}{D} \right)$$

where  $f$  is the focal length. The  $f/\#$  is given by  $\frac{1}{2NA}$  and also  $f/\# = \frac{f}{D}$ . NA is the numerical aperture of any optical system objective.

A 100 nm structure thus will not be able to be resolved in our CCD far field optical system operating in from 0.3 to 1  $\mu\text{m}$  range. In the realm of nanowires imaging, the resolution needs to be further reduced beyond the optical diffraction limit. One way of overcoming this is to use near field optical collection.

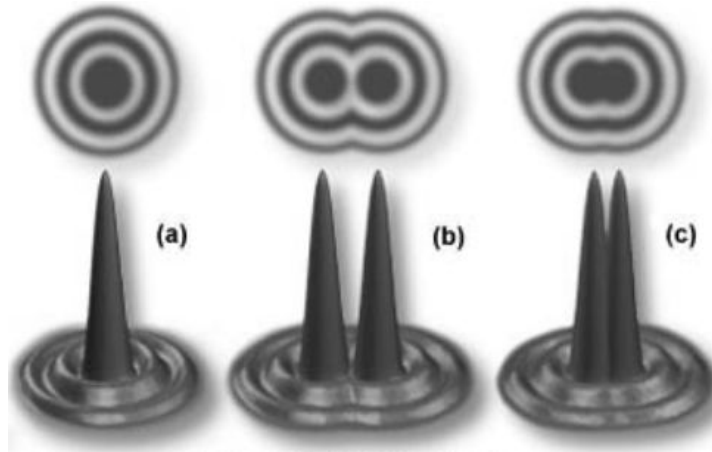


Figure 17. (a) Single resolvable sources, (b) Two sources still resolvable at  $2R$  apart, and (c) Two sources barely resolvable at  $R$  apart (from [27]).

## B. ATOMIC FORCE MICROSCOPE (AFM) AND NEAR FIELD SCANNING OPTICAL MICROSCOPE (NSOM)

### 1. AFM

The AFM is a very high-resolution type of scanning probe microscope, with resolution on the order of a nanometer, three orders of magnitude better than the optical diffraction limit. It may not be fair to compare AFM with optical microscope because of their totally different type of detection. AFM detects surface topography and what we see is the processed image of the surface. Typically, an AFM consists of a microscale cantilever with a sharp tip (probe) at its end that is used to scan the specimen surface. The cantilever is typically silicon or silicon nitride with a tip radius of curvature on the order of nanometers. When the tip is brought into proximity of a sample surface, forces between the tip and the sample lead to a deflection of the cantilever according to Hooke's law, hence the term 'atomic force'. Not only mechanical contact force is at work when the cantilever is very near the surface. At these small distances, other forces can include:

1. Van der Waals forces
2. capillary forces
3. chemical bonding
4. electrostatic forces
5. magnetic forces
6. Casimir forces
7. solvation forces

There are several methods used to detect these forces. Commonly, the deflection is measured using a laser spot reflected from the top of the cantilever. Other methods include capacitive sensing or piezoresistive cantilevers and optical interferometry. A feedback mechanism is needed to adjust the tip-to-sample distance as it scans the surface x-y plane and to maintain a constant force between the tip and the sample.

Instead of measuring deflection or force directly, the probe can also be mounted on a tuning fork, which oscillates at its resonant frequency. Changes to the amplitude, phase and resonance frequency are monitored as the tip moves over the surface [28]. Traditionally, the sample is mounted on a piezoelectric stage that can move the sample in the z direction for maintaining a constant force, and the x and y directions for scanning the sample. Alternatively a 'tripod' configuration of three piezo crystals may be employed, with each responsible for scanning in the x, y and z directions. The piezo x, y and z data are reconstructed to form a topography image. Figure 18 shows a topography image on a calibration grid reconstructed from the x, y and z data.

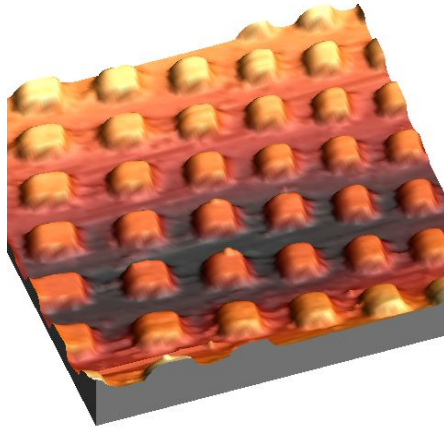


Figure 18. AFM topography image of a calibration grid 50  $\mu\text{m}$  x 50  $\mu\text{m}$ . The periodicity of the grid is 10  $\mu\text{m}$  and the islands are 100 nm tall.

## 2. NSOM

The mechanics of the AFM also offers a convenient platform to operate a near-field optical microscopy (NSOM) probe. Indeed, AFM coupled with NSOM capability is now common in the market. NSOM is based upon the detection of non-propagating evanescent waves in the near-field region. The near-field region is defined as the region away from the sample that is less than the wavelength of the incident light. This distance is typically on the order of a nanometer. In order to achieve an optical resolution better than the diffraction limit, an optical fiber probe is brought within the near-field region, or even in contact with the sample's surface. The probe can detect in the near-field directly by using the probe as a wave guide with a sub-wavelength size aperture. Light is collected at the other end of the fiber and is amplified and detected using an avalanche photodiode (APD). Typically in NSOM, laser light is fed to the aperture via an optical fiber to excite the luminescence. The aperture can be a tapered fiber coated with a metal (such as gold).

In this thesis, a specialized NSOM is used. Recall that for transport drift analysis, we need to retain the spatial information during cathodoluminescent emission from a point source. In conventional NSOM, the light collection probe is

fixed and scanning is achieved by moving the sample. Optical NSOM uses laser excitation via the fiber, so the generating source is co-located with the collection. This is that same as with the CL system on the SEM. The resulting image maps luminescence to the point of generation and collection, and drift information is lost. In a conventional NSOM, it would be impossible to keep a fixed charge generation point on the sample.

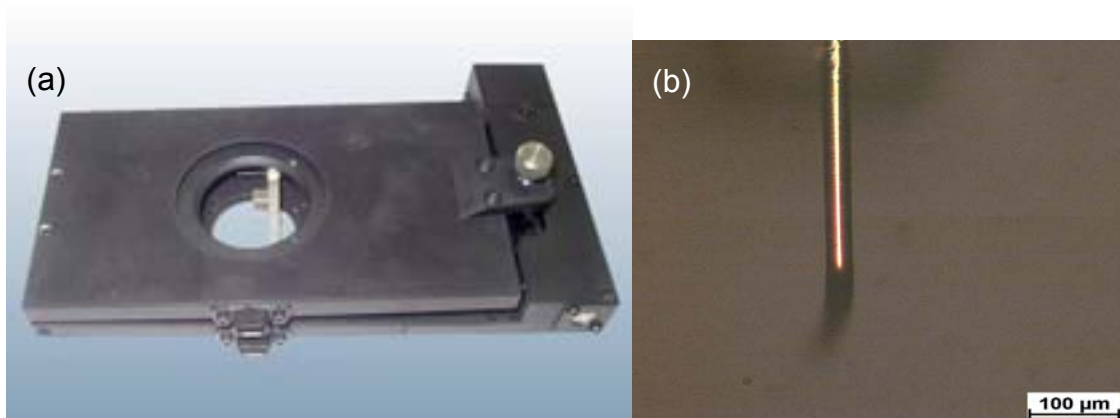


Figure 19. (a) Nanonics Multiview 2000 AFM/NSOM flat scanners (from [29]),  
(b) Optical image of the NSOM tip

Figure 19 shows the Nanonics dual scanning system and the NSOM open aperture tip. The AFM/NSOM by Nanonics enables independent x-y-z movement of both the sample and the probe. Now, we are able to fix the generating source on the point of interest and allow the tip to perform raster scanning on the potential drift area (Figure 20). Each scanner (probe and sample stage) has a range of 70  $\mu\text{m}$  in the x-y direction and 35  $\mu\text{m}$  in the z direction [30].

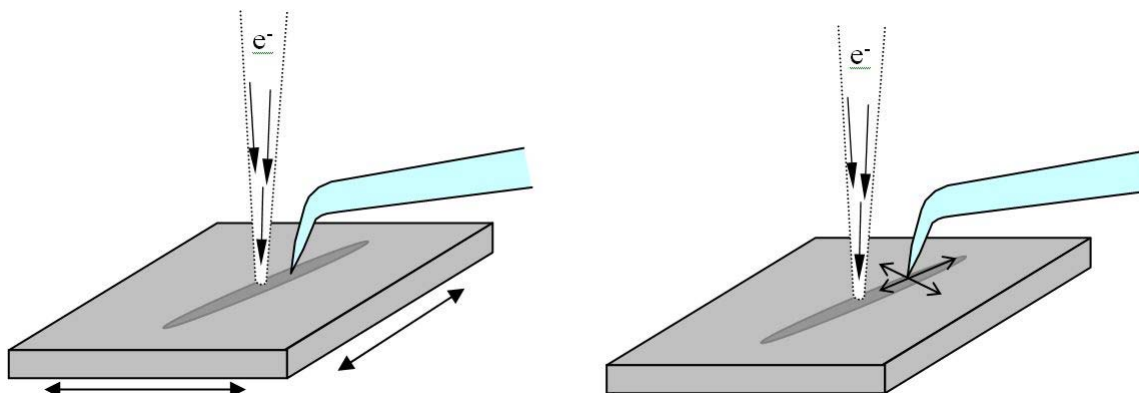


Figure 20. (Left) Fixed electron beam and probe, sample moves in x-y plane.  
(right) fixed electron beam and sample, probe moves in x-y plane.

In our experiment, the goal is to create electrons at a spot on the wire in the SEM and use the probe to scan along the wire to look for evidence of minority carrier transport. The Nanonics AFM/NSOM also has an interesting feature. It has the ability to perform inertial motion on the sample stage. The sample can be stepped in the x-y direction for 'long' distances to move the area intended for study under the probe.

### C. DATA EXTRACTION AND ANALYSIS

MATLAB was primarily used in the analysis of the CL, OM and AFM/NSOM data. Most images come in 2D raw image (TIF and BMP) and generally represent light intensities over a 2D plane. Basic image processing techniques are employed to filter pixel and background noises. Programs were written to automate the extraction, calculation and presentation processes. With the AFM data, a special routine is also written to filter out the slanted artifact when a sample is not perfectly mounted horizontally. The Nanonics WSxM image processing software is also used to provide advanced capability in image and data processing. The Annex lists some of the MATLAB programs written for this thesis work.

## 1 Obtaining the Diffusion Length from Experimental Data

The technique used for the extraction of diffusion length from experimental intensity distributions is described in previous work [6]-[7], [22]. The basic idea is that, in the far  $x$  region (for 2D samples,  $x \gg \sim 5L$ , where  $L$  is the diffusion length), we can approximate the intensity distribution as

$$I(x) \approx e^{-Cx}$$

where

$$C = \left( \frac{e}{2kT} \right) E - \sqrt{\left( \frac{e}{2kT} \right)^2 E^2 + \frac{1}{L_{diff}^2}}.$$

If there is no applied electric field ( $E=0$ ), then the intensity distribution is approximately  $I(x) \approx e^{-\frac{x}{L}}$ . So, using a semilogarithmic plot of  $I(x)$ , the slope is found using linear regression (Matlab) algorithm. The inverse of the slope is thus the estimated diffusion length. For relatively larger wires, this technique is expected to be a good approximation as with the 2D samples. However, for smaller wires, there exist other difficulties that have been discussed earlier in Chapter 2.

THIS PAGE INTENTIONALLY LEFT BLANK

## IV. STUDY OF NANOWIRES

### A. IMAGING OF ZNO NANOWIRES

#### 1. CL Measurements

Prior to transport imaging with the OM, the first step is use CL to determine the luminescence intensity and spectrum from a ZnO nanowire. The wire used in this experiment is sample 'A' of a set of ZnO wires fabricated by the Molecular Foundry at LBNL. The ZnO nanowires are produced using a vapor phase transport process. The wires on the sample are approximately 5-10  $\mu\text{m}$  long with various diameters randomly deposited on the substrate. There are 2, 5 and 10  $\mu\text{m}$  gap devices (metal contacts) deposited onto the substrates. Metals are deposited to attempt to isolate single wires spanning a contact, to create a simple 2 terminal device. The first panchromatic CL image of a group of wires at 5000X is shown in Figure 21.

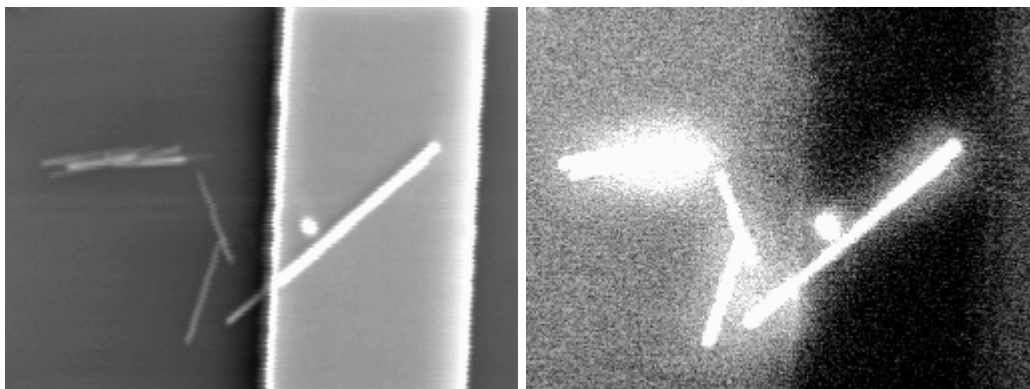


Figure 21. SEM micrograph (left) and CL image (right) of a group of ZnO nanowires on both Si and metal regions at 5000X.

Luminescence is observed at the brighter region. This clearly reflects orientation of the randomly deposited wire. Luminescence is also observed from

the SiO<sub>2</sub>/Si substrate. A CL spectrum was taken by choosing the excitation spot to be placed either directly on wire or on the substrate region. Peak intensity for the luminescence from the wire is at 376 nm. With a band gap of 3.37 eV at room temperature, the spectra peak is in the range expected for ZnO.

$$\lambda(\mu m) = \frac{1.24}{E_{bandgap}(eV)} \approx 368nm$$

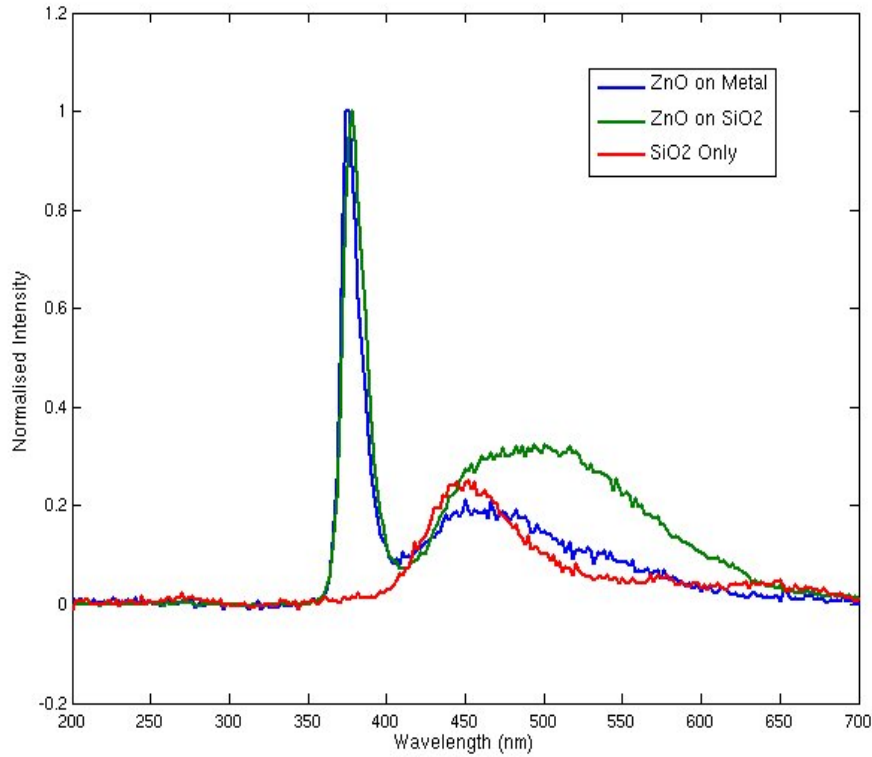


Figure 22. CL spectra of ZnO nanowire and its substrate.

Figure 22 shows the luminescence spectra of ZnO wire (on metal), ZnO wire (on SiO<sub>2</sub>) and SiO<sub>2</sub>/Si only substrate. Both ZnO spectral are normalized to its peak.

## 2. Effect of Size on ZnO Nanowire Luminescence

The abrupt discontinuity of the lattice structure at the surface can result in the introduction of a large number of recombination centers. These surface states can greatly enhance the recombination rate at that region. The dependence of surface recombination on the size of nanowires has been reported [4]. Surface states can be associated with a very few monolayers of the sample. Within this thickness, carriers can diffuse to the surface before they recombine. If we assume thickness  $t$ , and the probability of recombination is 1, then the volume associated with surface recombination is

$$S_{surf} = l\pi \left[ r^2 - (r-t)^2 \right]$$

where  $r$  is the radius of wire and  $l$ , its length, is  $\gg r$ . The remaining bulk volume of the wire is

$$S_{bulk} = l\pi (r-t)^2$$

Taking the ratio of the volumes,

$$\frac{S_{bulk}}{S_{surf}} = \frac{r^2}{2rt - t^2} - 1$$

The above equation also suggests that the ratio of the volumes are nearly linear with the radius of the wire. Let's assume that band-edge and below-band-gap peak luminescence is associated with bulk volume and surface volume respectively. If we also assume that the volume ratio is a dominant factor by comparison, we have

$$\frac{I_{bulk}}{I_{surf}} = C \left( \frac{r^2}{2rt - t^2} - 1 \right)$$

where  $C$  is a pre-factor taking into account the process efficiencies of luminescence and the collection equipment. This model predicts that the ratio of  $\frac{I_{bulk}}{I_{surf}}$  will decrease if  $r$  is reduced substantially. This has been experimentally observed by Shalish et.al [4] and is illustrated in Figure 23.

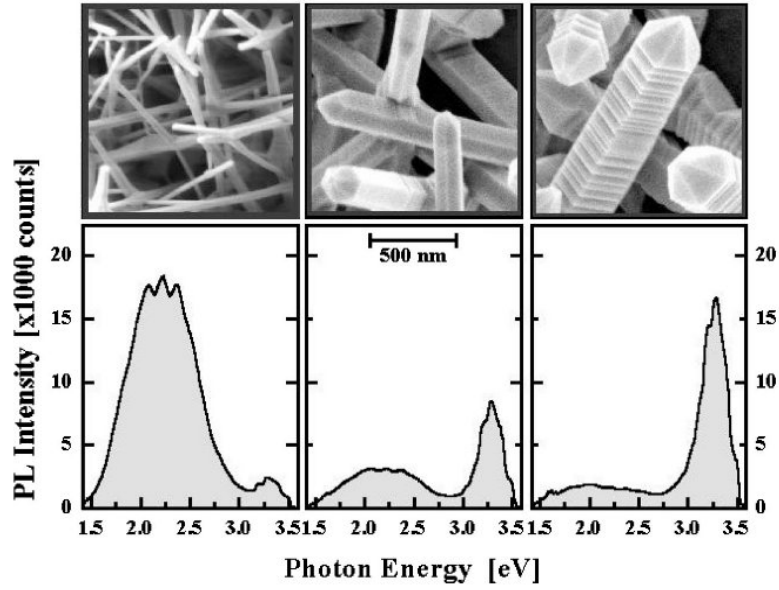


Figure 23. PL spectra obtained from ZnO wires of three different sizes (from [4]).

A similar result is observed in our CL measurement (Figure 24). The wire we imaged is on the order of 500 to 800 nm in diameter and shows similar  $\frac{I_{bulk}}{I_{surf}}$  ratios. To retain the bulk luminescence of our ZnO nanowire for which the band-edge luminescence is  $\sim 380$  nm, we used a bandpass filter to extract the bulk ZnO signal for analysis. This removed the luminescence from the substrate, as well as the surface related CL and improved the signal to noise for detection of individual wires.

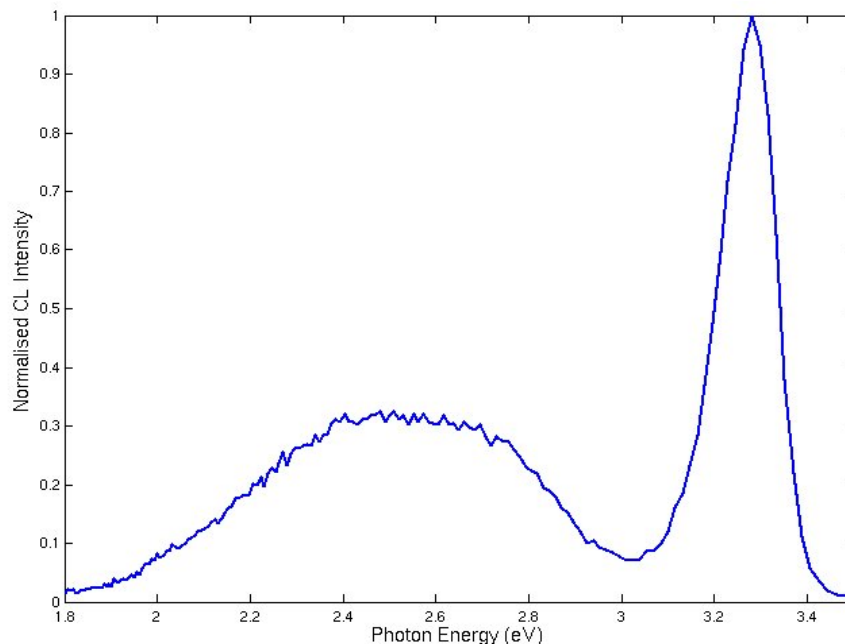


Figure 24. CL intensity spectra of a ZnO wire approximately 500 nm in diameter

### 3. CL Measurements with Band Pass Filter

First, CL imaging using the monochromator and PMT was conducted on a single wire. Figure 25 shows a SEM micrograph and CL image of the ZnO wire at 5000X with dimensions approximately 0.4  $\mu\text{m}$  across and 8  $\mu\text{m}$  long.

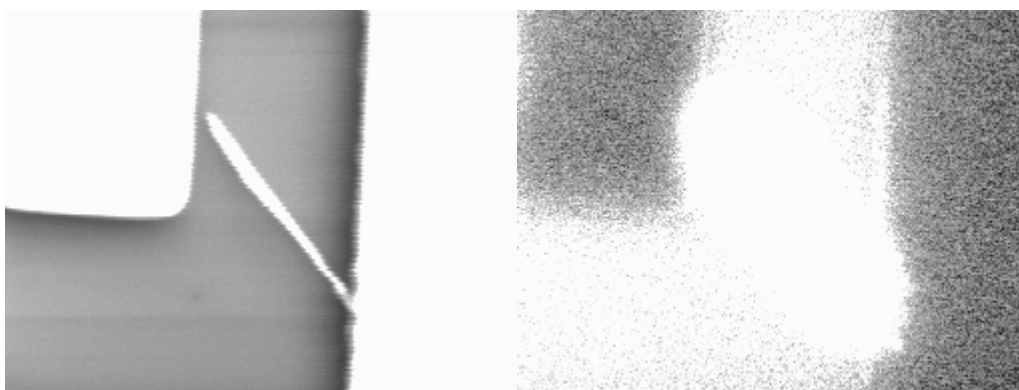


Figure 25. SEM micrograph (left) and CL image (right) of a single ZnO wire at 5000X.

The dark region in the SEM image is the substrate while the brighter region is a metal contact. The CL image shows bright luminescence from a broad region in a conventional CL panchromatic measurement. In panchromatic mode, all collected light is directed to the PMT, eliminating the monochromator from the optical path. The monochromator is then used to select light of  $\sim 380$  nm to extract the ZnO's bulk emission. In Figure 26, the band-edge luminescence from the ZnO wire is clearly captured.

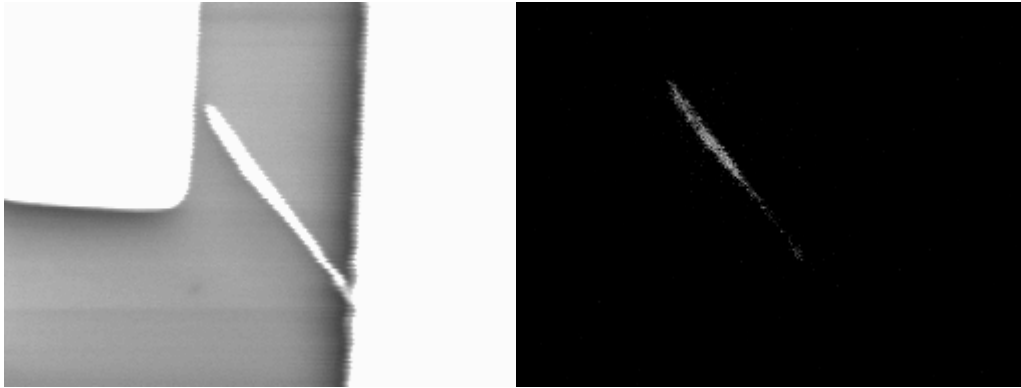


Figure 26. SEM micrograph (left) and CL image (right) with  $\lambda = 380$  nm for a ZnO wire (5000X).

The same CL measurement is taken with the same wire and identical experimental conditions. Only this time the magnification is increased to 15000X (Figure 27).

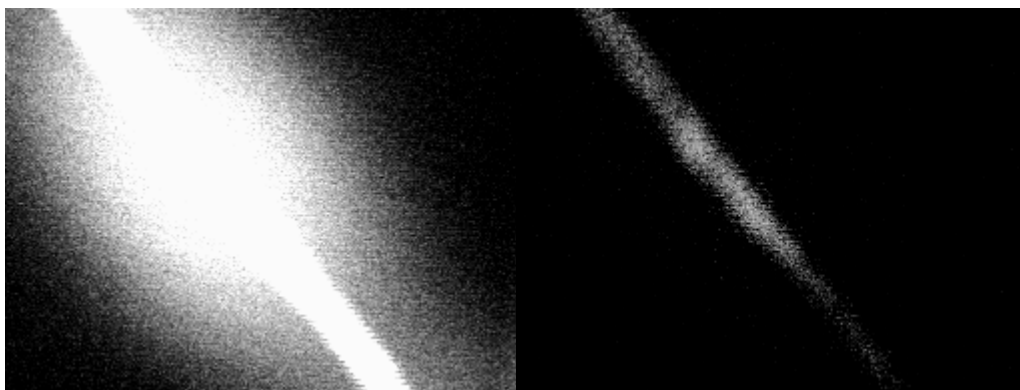


Figure 27. CL image panchromatic (left) and with  $\lambda = 380$  nm (right) at 15000X.

The diameter of the wire is not uniform along its length. The peak band-edge luminescence is observed to vary with the radius of the wire. This reflects the role of the surface recombination, as discussed in Section 2.

#### 4. OM Measurements

Based on the information from the CL spectroscopy, a 380 nm optical band pass filter was installed on our OM system. It has a bandwidth (FWHM) of  $10 \pm 2$  nm. It was inserted right before the CCD-camera shutter. The first images were of a group of ZnO wires on sample A.

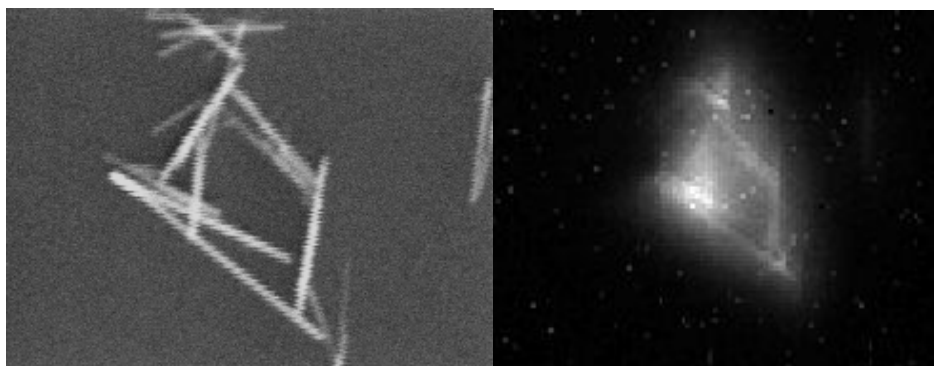


Figure 28. SEM micrograph (left) and OM scan mode image (right) on ZnO wires at 5000X.

The wires on the SEM picture measure about 8-10  $\mu\text{m}$  in length and 0.5  $\mu\text{m}$  in diameter. The OM image shows promising results and clearly displays the pattern of the wires (Figure 28). The light signal on the camera (after the filter has been installed) was weak and the image is taken over an extended integration time (100 sec) that can be controlled by the camera shutter. Figure 29 shows the results of a single wire in scan mode.

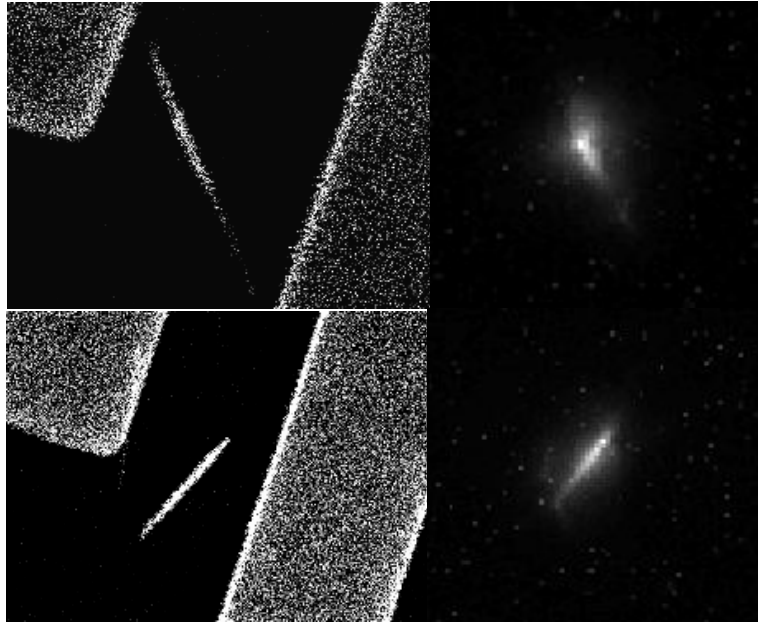


Figure 29. OM images of single ZnO wires with 380-bandpass filter (the 2 left images are SEM micrographs of the corresponding wires) at 8000X.

Note that the CCD image is beginning to pixelize as the magnification gets larger. With the OM resolution of 0.4  $\mu\text{m}$  per pixel, the emission from the wires essentially only occupies 1 or 2 pixels across! This reflects the quasi-1D nature of the system, as well as the resolution limit of the far field optical system. Fortunately, along the wire, there will be about 10-20 pixels from excitation along the full length.

For carrier transport analysis, we need to introduce a quasi-point source to generate charges. The SEM spot-mode is used and the electron beam was

positioned to hit directly onto the wire. Figure 30 shows spot mode results for single wires of about 400 nm in diameter and 5-6  $\mu\text{m}$  in length. The beam position is difficult to control precisely at this scale using the SEM. By trial and error, we will know if the beam is fully incident on the wire. If the beam hits the substrate, the luminescence differs substantially.

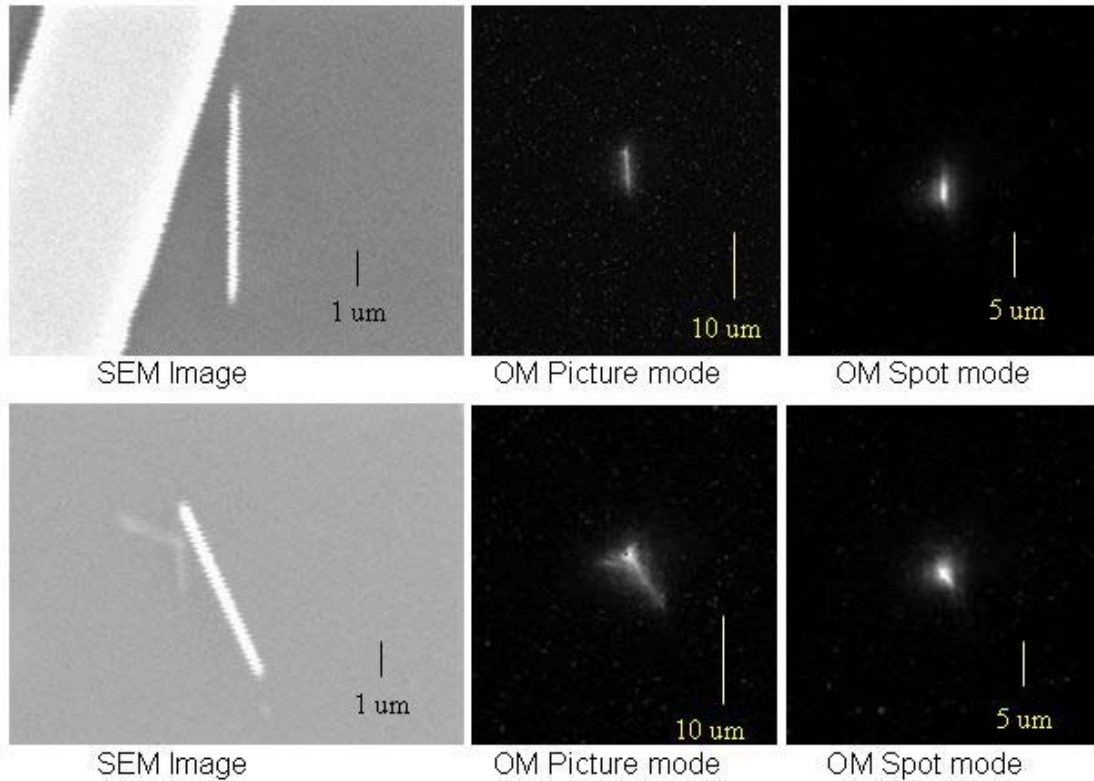


Figure 30. SEM scan and spot modes images of 2 different wires (Probe current =  $1 \times 10^{-10}$  A, 20 keV).

The elongation on the spot-mode images is along the wire's long axis. This suggests that there may be carrier diffusion along the wire. The beam width used is about 50 nm in diameter, much smaller than the measured luminescence distribution along the wire. If carrier motion is the source of the distribution (as opposed to electron beam scattering or substrate interaction), then the diffusion length  $L$  can be obtained.

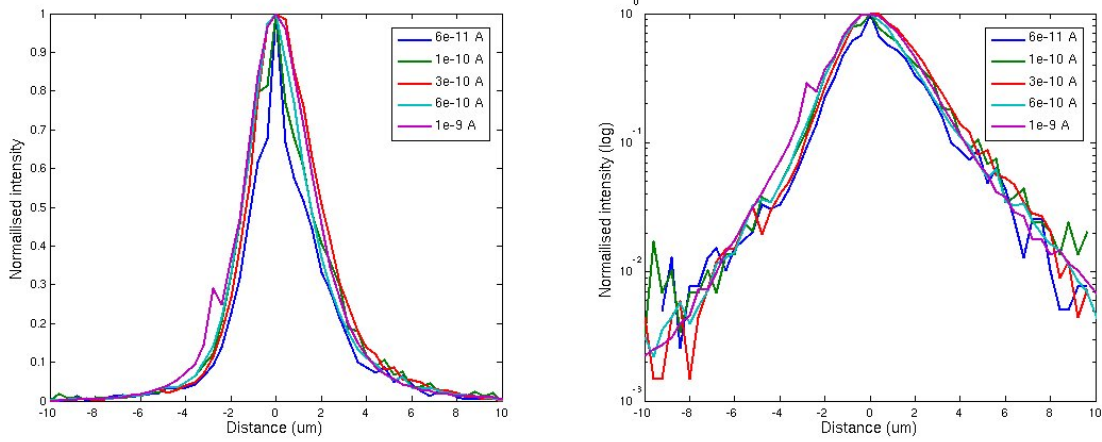


Figure 31. Intensity distribution along the wire (spot mode) with varying electron beam probe current.

The intensity distribution from the OM image along the wire in spot-mode excitation is extracted. Figure 31 shows the normalized intensities along the wire with varying probe current at 20 keV. The result shows consistent intensity distributions – and on the semilogarithmic plot the slopes are almost the same. The lateral extent of generation region (shape of the peak) is slightly affected by the changing probe current. This can be expected as the electron beam spot size varies with probe current from ~50 nm to ~150 nm [21]. Considering the wire to be in the order of 300nm in diameter, the spot size is relatively significant. The insensitivity of the intensity distribution to varying probe current demonstrates that these results are in low excitation limits [21]. This suggests that the intensities imaged are from minority carrier recombination in an approximately constant majority carrier distribution. In the semilogarithmic plot, the slope of the distribution at a point beyond the generating region approximately reflects the material diffusion length  $L$ . The results for different probe current displayed minimal variations in the semilogarithmic plot slopes and hence consistent diffusion length. This is expected, as the diffusion length should not depend on generation rate at the excess carrier source.

A similar measurement is taken with a  $6 \times 10^{-10}$  A probe current at 20 keV. The line intensities along the wire and across the wire are shown in Figure 32. The lateral generation region of line intensity along the wire is much broader than that of across the wire. This can be attributed to the relative size of wire with the electron beam size. Carriers from the generation region are confined (in space) more across the wire than along it. The slope obtained from across the wire (perpendicular to wire) provides the absolute limit of the technique using the optical microscope.

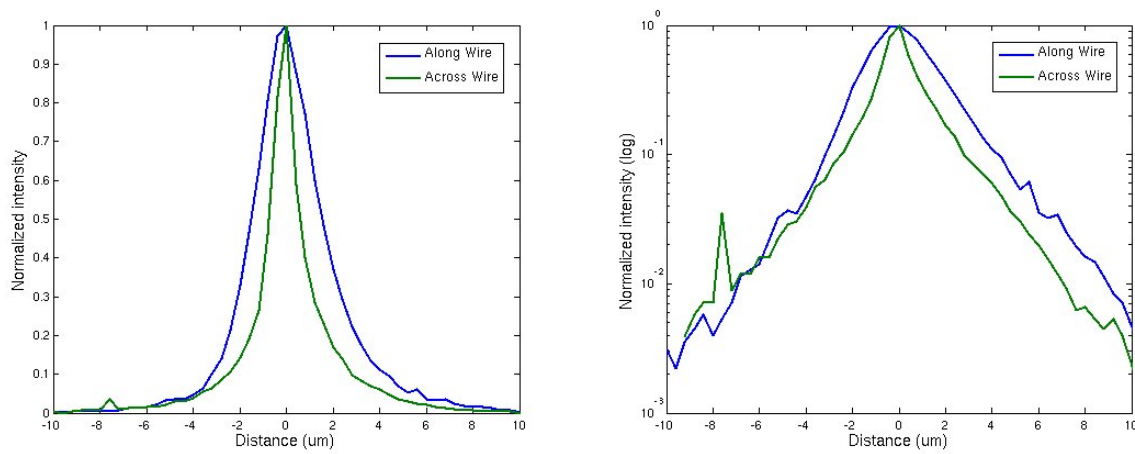


Figure 32. Intensity distribution along and across the wire at probe current  $6 \times 10^{-10}$  A.

Again, the semi-logarithmic plot shows approximately common slopes in the 'far' region. Obtaining the slopes from the plots, using  $L = \frac{1}{\text{slope}}$  in the absence of an electric field, we find the values tabulated in Table 2. .

	Measured Diffusion Length (1/slope)	Region that the slope is determined
Along wire 1	1.69 $\mu\text{m}$	+ 3 $\mu\text{m}$
Along wire 2	1.72 $\mu\text{m}$	+ 3 $\mu\text{m}$

Table 2. Measured Diffusion length for wire 1 and 2

The technique presented in this section is approaching the resolution limits. The diffusion length presented in Table 2 may not truly represent diffusion length of minority electrons. In bulk ZnO materials, diffusion length of minority holes has been measured to be about approximately 440 nm [31] at room temperature. A logical hypothesis will be that the diffusion length of ZnO nanowires will be less than that of ZnO bulk material. Transport measurements on individual nanowires are still very limited [31]. A very recent measure of majority carrier mobility in ZnO nanowire FETS gives a mobility of only 2-4 cm<sup>2</sup>/Vs [32]. With a lifetime of  $\tau \sim 10^{-9}$  s, this would result in a diffusion length of 70 -100 nm.

## B. MODELING ZINC OXIDE NANOWIRES

In the thesis work, one of the difficulties of measuring transport is the relatively short diffusion length that we expect to measure. For a pure diffusion length measurement, there is no applied field. The luminescence intensity falls very quickly in  $x$  when  $L$  is less than 1  $\mu$ m. Measurement at this scale approaches the limits of the OM system where the size of 1 pixel of any captured image is 400 nm. To simulate with realistic values of diffusion length, the numerical solution is used (Chapter II, Section C1).

$$I_{ss} = \frac{g}{\sqrt{S^2 + 4L^2}} \sqrt{\frac{m}{\pi}} \int_{-\infty}^{\infty} e^{-\left[ m\xi^2 - \frac{S(x-\xi)}{2L^2} + \frac{|x-\xi|\sqrt{S^2+4L^2}}{2L^2} \right]} d\xi$$

Assuming a diffusion length of 300 nm and a generation region of 100 nm (side length in 1-D), a series of simulations are made for several values of applied field. For a inter-contact distance of 10  $\mu$ m, if a bias is applied at 1 V, then the electric field will be 1000 V/cm. Figure 33 shows the predicted intensity distribution from the simulated 1-D model.

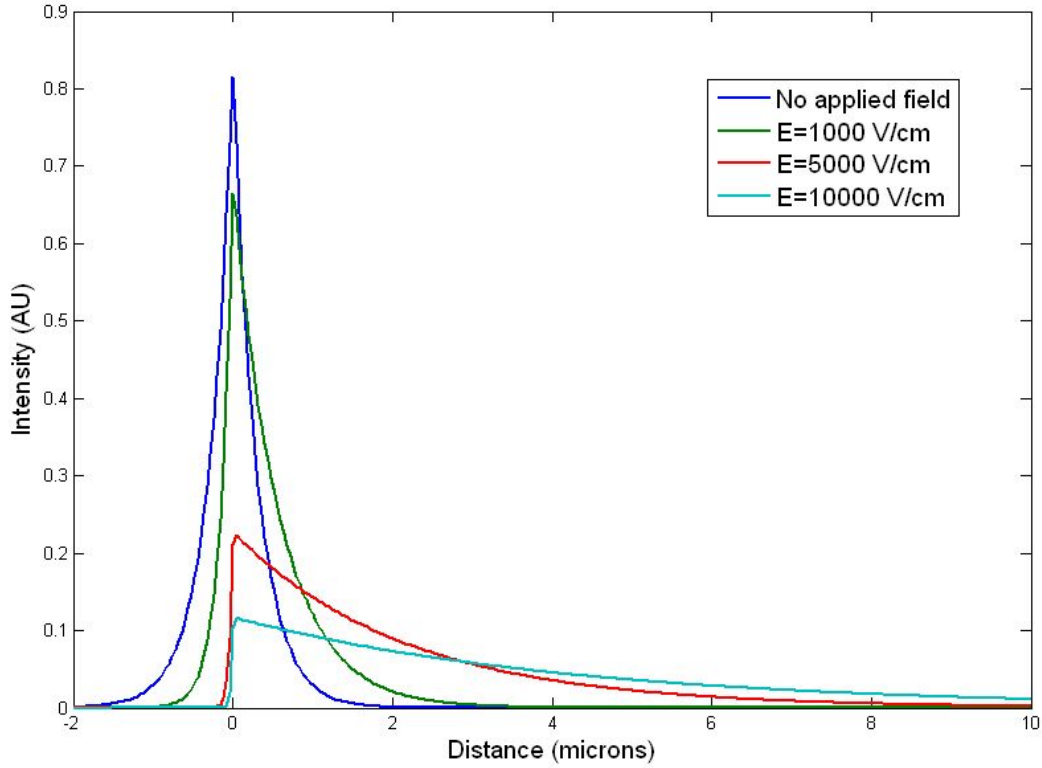


Figure 33. Simulated recombination intensity profiles of a 1-D material,  $L=0.3 \mu\text{m}$ ,  $m = 8000 \mu\text{m}^{-1}$  (generation region side length = 100 nm), for several values of electric field.

From the simulation results in Figure 33, the intensity distribution due to drift effects can be mapped beyond  $6 \mu\text{m}$ . At this distance, measurements can be made using the OM system, but can only be fully resolved with near field imaging.

Applying an electric field onto a single nanowire represents a step beyond the current experiments. It will require special fabrication facilities to connect biasing contacts to an external power supply once a single intact wire can be found bridging across the two contacts. In the current work, the focus is to take the first step of measuring carrier transport without applied electric field. In this case, the near field optical system is still required.

THIS PAGE INTENTIONALLY LEFT BLANK

## V. INSTALLATION AND OPERATION OF AFM/NSOM

### A. OPTIMIZATION OF AFM/NSOM SCAN QUALITY

Scanning at the nano-scale requires control of vibration, scan tip quality, sample quality and surface forces at a level far beyond that required at the macro or even micro ( $\mu\text{m}$ ) scale. Getting the dedicated equipment work consistently at optimum quality is a challenge by itself. Many parameters and variations affect the image quality and reproducibility. It is important to understand these effects in order to interpret results from these scans. Therefore, a series of control measurements must be performed. Before beginning measurements on nano-scale wires, we used a calibration grid and some strongly luminescent epitaxial samples in a series of exploratory experiments. Figure 34 shows an NSOM image of a GaAs heterostructure. The bright region is the semiconductor while the dark region is the metal contact area. This demonstrates the first NSOM collection of electron-beam-induced luminescence in the system.

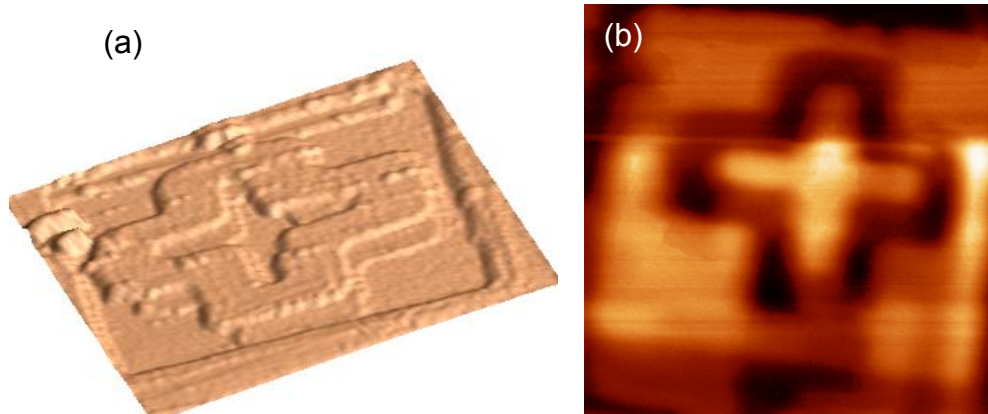


Figure 34. (a) AFM topography image of a GaAs structure  $40\ \mu\text{m} \times 40\ \mu\text{m}$ . (b) the corresponding NSOM image.

The NSOM image shown in Figure 34 was scanned using the bottom scanner in x-y-z axis. The electron beam is displaced about 1  $\mu\text{m}$  from the tip. In this scan, the relative position of the tip and the electron beam is held fixed.

### 1. Tip Integration Time

Tip integration time refers to the duration the tip stays on one point on the sample before moving to the next. The Nanonics system requires a minimum of 1 ms [30] due to system time constants. The default is set at 8 ms for optimum scan quality. It is found that for AFM scans from a comparison of 10 ms and 20 ms tip integration time, the quality of scan does not differ appreciably (Figure 35). The time taken for the 20 ms scan is twice as much as the 10 ms scan.

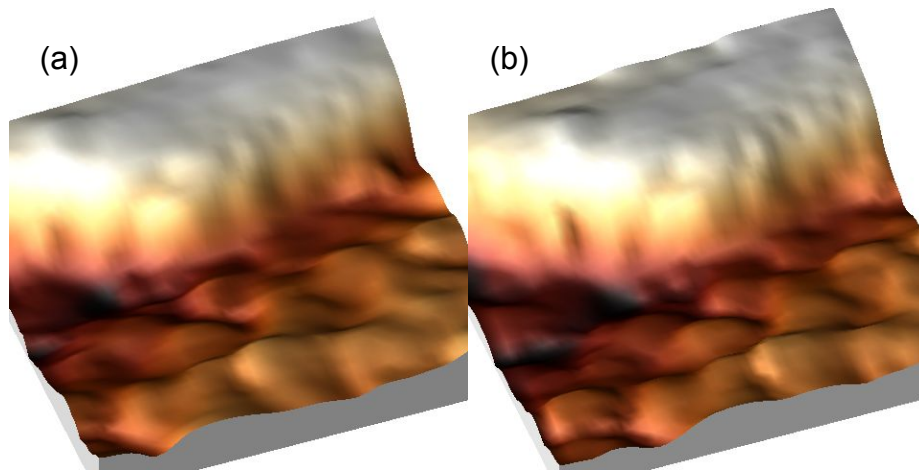


Figure 35. AFM scans on the edge of a 100 nm tall structure 20  $\mu\text{m}$  x 20  $\mu\text{m}$ .  
(a) tip integration time 10 ms, (b) 20 ms.

However, the main merit of longer integration time is believed to be the ability to collect a higher NSOM signal from weakly luminescent samples.

## 2. Upper Scanner and Lower Scanner

The unique feature of Nanonic's AFM/NSOM is that it has 2 scanners: top and bottom, while conventional AFM only has the bottom scanner. For normal AFM scans, this is transparent to the user. Scanning with either the top or bottom scanners yields approximately the same quality images. However, for NSOM measurements and particularly our type of transport experiment, we need to use the top x-y scanner to maintain a constant electron-beam position on the sample. Figure 36 shows the results of top and bottom AFM x-y scans. Although the details on the wire plateau seem better with the lower scanner, the other scans we did are generally similar. The ripples on the right side of the wires are artifacts due to the scan being traced left to right. From the 'retrace' images, the ripples appear on the left side. This can be eliminated by proper PID tuning.

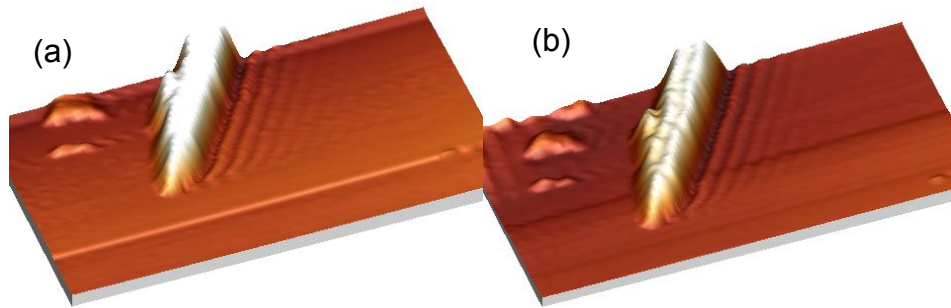


Figure 36. AFM scans of ZnO wire  $10\ \mu\text{m} \times 5\ \mu\text{m}$  (a) top scanner, (b) bottom scanner.

The Nanonics AFM/NSOM also allows a combination of top or bottom scanners with top or bottom z-axis feedback. While scanning with top x-y scanners, the best result we achieved is the bottom z-axis feedback. By using this combination, we are able to image a nice edge from a metal contact edge on a luminescent solar cell material (Figure 37). Note that the knoll is a feature on the material that can be observed with the SEM.

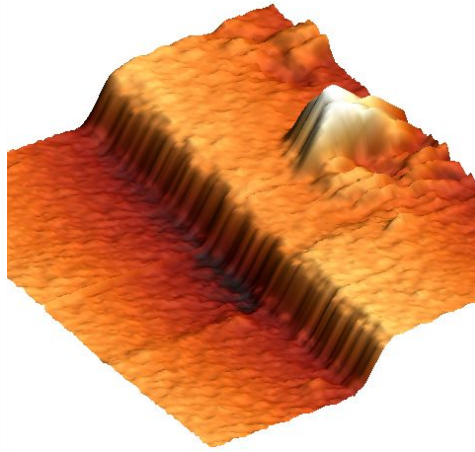


Figure 37. AFM scan on a solar cell contact edge about 200 nm tall ( $30\text{ }\mu\text{m} \times 30\text{ }\mu\text{m}$ ), using top x-y scanners and bottom in z feedback.

### 3. Amplitude Feedback Vs Phase Feedback

In general, phase feedback is preferred to amplitude feedback. Because it is detecting phase changes of the vibrating tuning fork, it offers a faster response and promotes less contact between the sample and the probe [30]. When working with phase feedback, less energy is required, decreasing the force of interaction between the tip and the sample and minimizing damage to the tip. However, phase feedback is not always used because of the Q factor of individual tip. 'Lower' quality tips or 'degraded' tips must use amplitude feedback, as they are much less sensitive than the phase feedback. In many cases, after a tip has been used for some time, we eventually have to use amplitude feedback. Figure 38 shows a comparison between amplitude feedback and phase feedback. The result for phase feedback shows a better image. The details of the substrate features are better captured by the phase feedback scans.

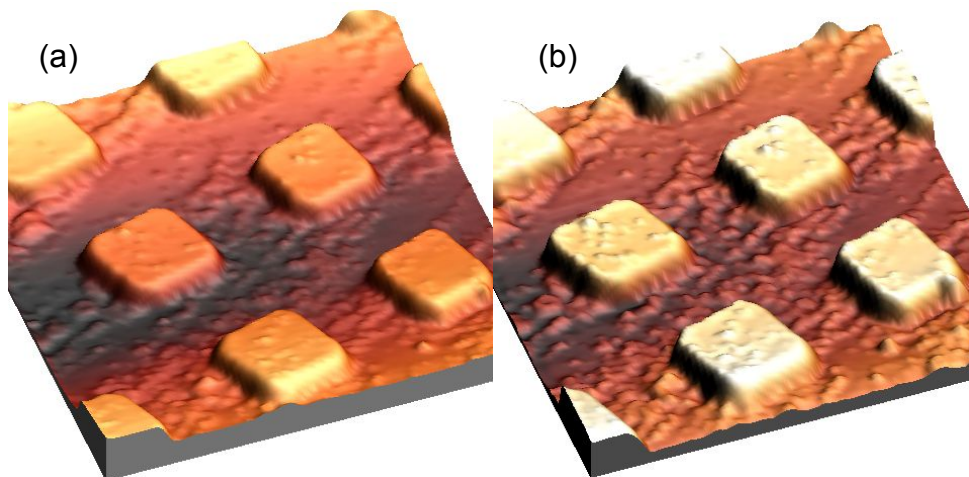


Figure 38. AFM scans on calibration grid  $20\ \mu\text{m} \times 20\ \mu\text{m}$ , with feature height of  $100\ \text{nm}$ , (a) using magnitude feedback, (b) using phase feedback.

#### 4. Feedback PID Controller

The PID feedback control offers a way to tune the feedback signal and control the system response to the feedback signal. It can be done by observing the line scans while the AFM/NSOM is conducting a scan. The integrator gain defines how fast a correction is applied to the scanner. The differential gain adds a negative or positive signal to the  $z$  correction. The proportional gain defines the magnitude of the correction signal [30]. Table 3 summarizes the effect of increasing these parameters.

Parameter	Rise Time	Overshoot	Settling time
Integrator	Decrease	Increase	Increase
Differential	Little Change	Decrease	Decrease
Proportional	Decrease	Increase	Little change

Table 3. Effect of *increasing* parameters.

Figure 39 shows how the PID feedback control can improve the topographical image quality of AFM scans. For any new tip installed and with different samples, PID tuning is required for optimum AFM scan quality.

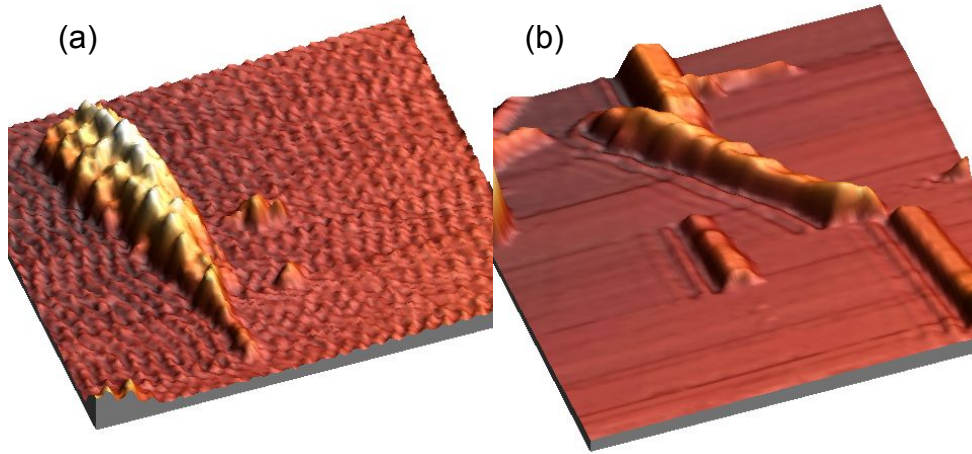


Figure 39. Effect of tuning the AFM PID feedback. (a) Initial AFM image of a wire  $20\text{ }\mu\text{m} \times 18\text{ }\mu\text{m}$ , (b) AFM image  $15\text{ }\mu\text{m} \times 15\text{ }\mu\text{m}$  with optimized PID feedback.

## B. AFM/ NSOM CALIBRATION

The x-y position and the z feedback signals are measured in voltages. Hence, there is a need to calibrate these signals to reflect actual distances and height. Experimentally, we used a Nanosurf calibration grid (BT00250). It has an x-y periodicity of  $10\text{ }\mu\text{m}$  and feature height of  $100\text{ nm}$ . The square islands shown in Figure 40 are  $5\text{ }\mu\text{m}$  by  $5\text{ }\mu\text{m}$ . To calibrate the scanners, the x-y and z multipliers are adjusted in the NWS1455 AFM/NSOM controller software until the scanned features reflect the known dimension of the calibration grid.

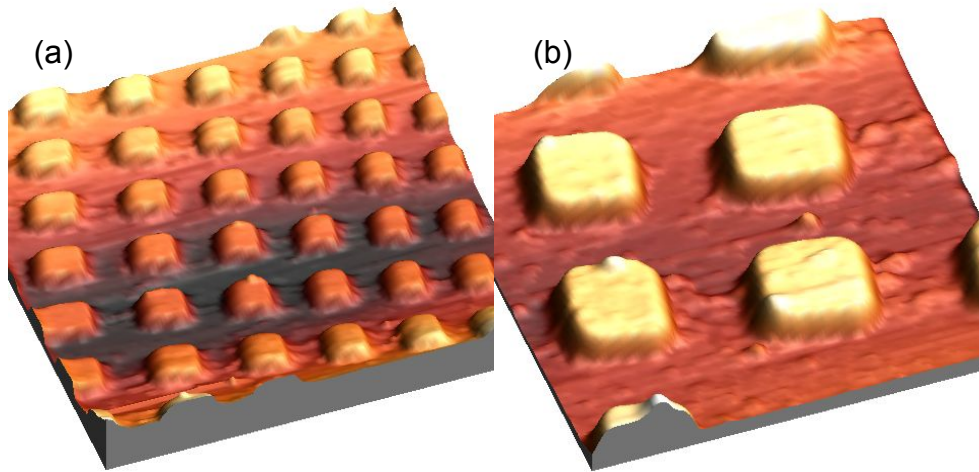


Figure 40. AFM scans calibration grid (a) 50  $\mu\text{m}$  x 50  $\mu\text{m}$ , (b) 20  $\mu\text{m}$  x 20  $\mu\text{m}$ .

### C. TOPOGRAPHICAL AND OPTICAL RESOLUTION

The physical resolution of the AFM is straightforward. For an AFM tip, the resolving power is determined by the size of the tip and its shape (usually 20 nm and inverted pyramid shape). The tip of the NSOM fiber varies from 150 nm to 500 nm. For a 250 nm tip (that is the aperture is 250 nm in diameter), the ideal resolution should be around 250 nm. This can be explained by a simple schematic (Figure 41). As the tip moves laterally pass an ideal edge (light emitting edge), the intensity of collected light through the tip rises until the entire diameter of the tip is over the edge. The curve of the intensity distribution can be estimated to be in the form of accumulative Gaussian distribution. The resolution can be determined by the lateral distance for the variation rate to rise from 10% to 90%. This is termed as ‘edge resolution’ [33]. So the ideal NSOM signal resolving power is on the order of 135 nm for a 250 nm tip.

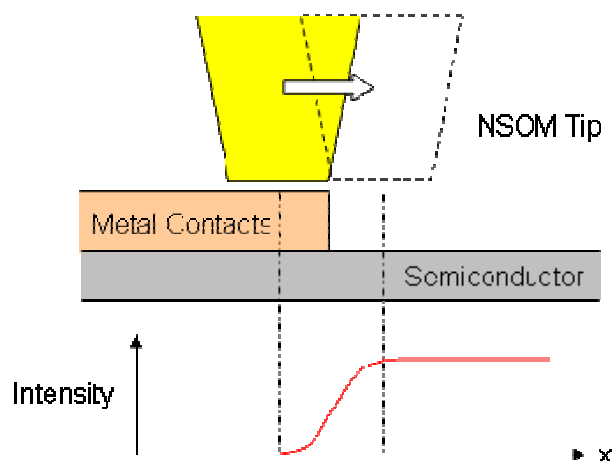


Figure 41. Illustration of an NSOM tip scanning over an ideal edge.

To test this, we used a 250 nm tip to image an edge feature of a forward biased solar cell. Under forward bias, the solar cell material emits light and the metal contacts do not. The height of the metal contacts is about 200 nm. Figure 42 shows the results of this experiment. For this edge, the edge resolution was found to be 2.2  $\mu\text{m}$ . The practical resolution is 10 times more than the ideal resolution! In this experiment, the edge of the solar cell is not a perfect edge as shown in the corresponding height profile (AFM topography). If the edge resolution is obtained from the apparent edge at 3.2  $\mu\text{m}$  (Figure 42) to 90% threshold, then the edge resolution is  $\sim 800$  nm.

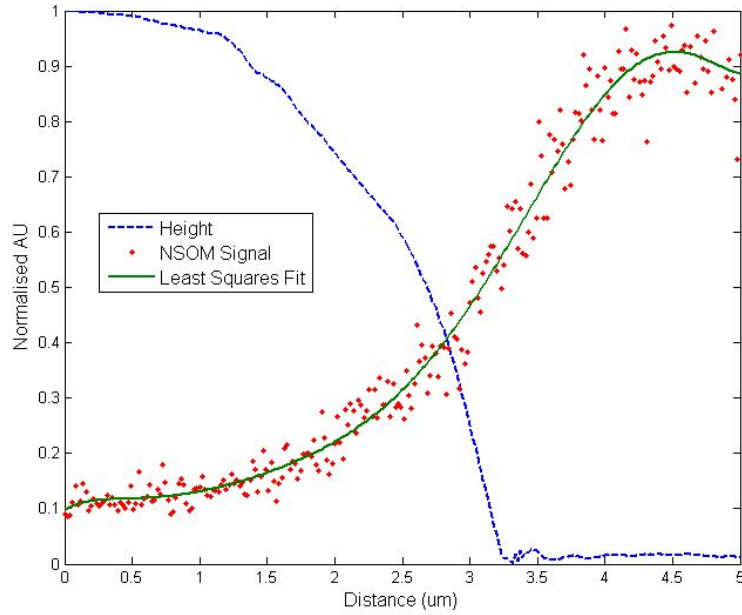


Figure 42. Topography and NSOM line scan of a forward biased solar cell.

This only describes a way to estimate the resolution of the NSOM. More work is needed to investigate the physical and NSOM resolution for tips of different sizes. Samples with brighter NSOM signals and better physical edges, i.e., sharp edges and shorter height must be used.

#### D. TIP AND CHARGES INTERACTION

The ultimate objective of this research is to image the luminescence intensity distribution along a wire resulting from a point source excitation of excess carriers. To achieve this, the electron beam (spot mode) has to be fixed on the wire while the scanning tip scans along the remaining length. The NSOM tip is made of  $\text{SiO}_2$  (a standard optical fiber) and hence in the presence of electrons, it accumulates charge since it is an insulating material. The charges on the tip are found to be significant and this severely affects the steering of the electron beam.

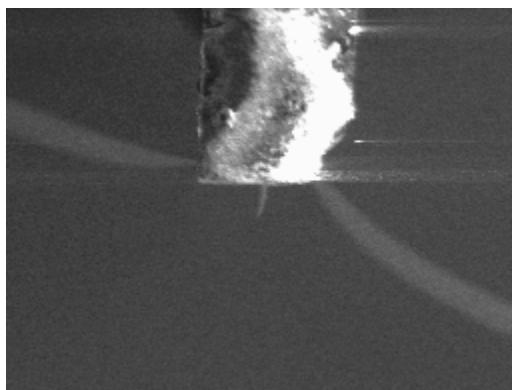


Figure 43. SEM image of an NSOM tip on the tuning fork. Note the distorted structure due to charging.

Figure 43 shows how an SEM image of a straight structure can be distorted by the fields associated with charging. The scanning electron beam around the tip is deflected, providing a distorted image. As the dimension of a wire is small, to hold the electron beam steady on the wire is especially difficult. To mitigate this effect, the tip is coated with gold to conduct away excess charge. The coated tip still shows signs of beam interaction. Nanonics is currently working to improve its tip design. This includes better tip coatings and also eliminating astigmatism by changing the magnetic mount that attaches the tuning fork to the top scanner. A second generation top scanner is being produced and will be installed in December 2007 to address this effect.

## VI. IMAGING OF NANOWIRES USING AFM AND NSOM

### A. NANOSCALE FEATURES OF ZINC OXIDE WIRES.

The ZnO nanowires on Sample A were imaged with a high resolution, low keV SEM (MySEM) at NovelX laboratory. Figure 44a shows good details of small individual wires clustered together. These were previously thought to be thicker wires. In Figure 44b, a single wire about 100 nm in diameter was imaged. The SEM image shows a region of interaction between the wire and the substrate.

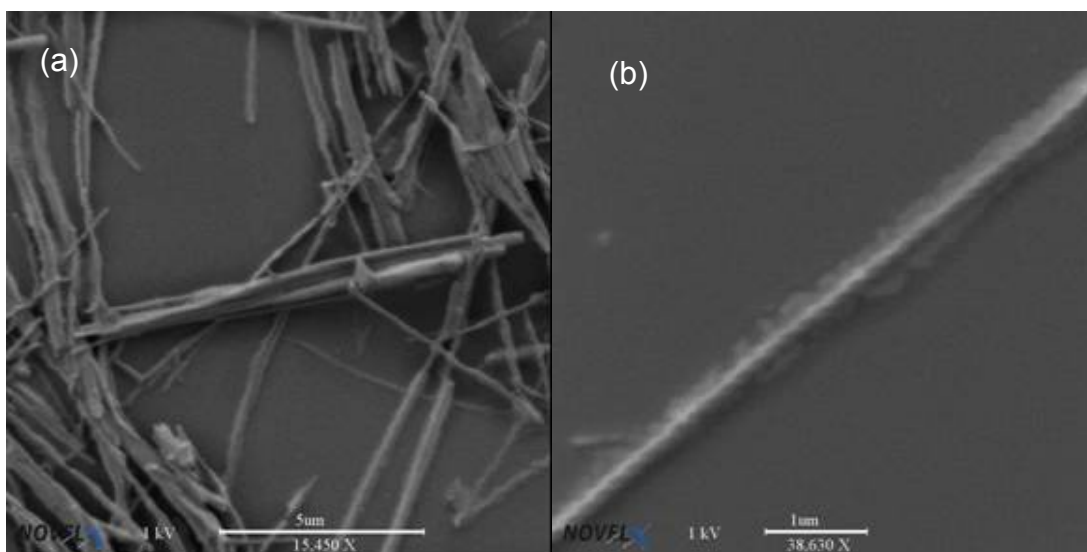


Figure 44. (a) SEM image of ZnO wire cluster, (b) Image showing some interaction between the wires and substrate

In our AFM scans on a similar area of sample A, a 200 nm AFM/NSOM tip is used. The features of the cluster are clearly seen in Figure 45. The tip is able to resolve height features of less than 400 nm. The interaction at the substrate is also visible.

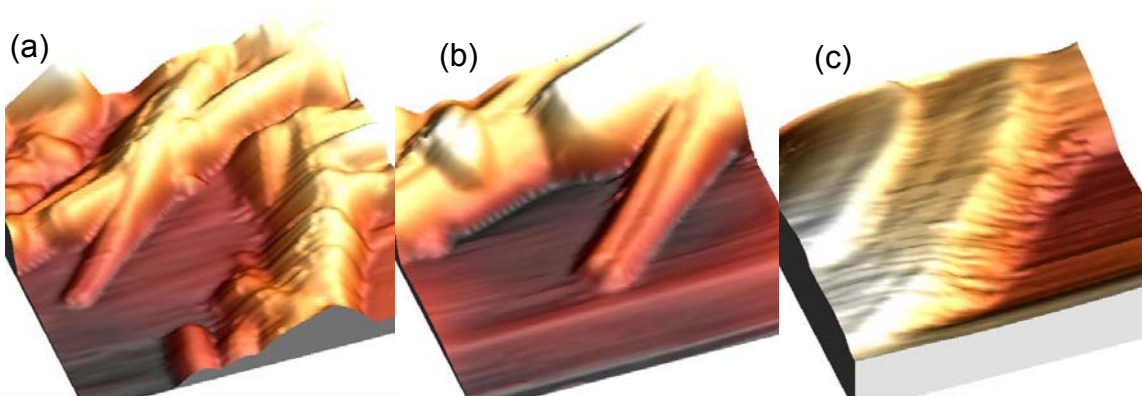


Figure 45. AFM topography image of ZnO nanowires. (a)  $10\ \mu\text{m} \times 10\ \mu\text{m}$ , (b)  $5\ \mu\text{m} \times 5\ \mu\text{m}$ , and (c) zoomed down to  $1\ \mu\text{m} \times 1\ \mu\text{m}$ .

## B. “FIRST LIGHT”

The collection of light from a cluster of ZnO wires was performed using a 500 nm tip. The tip has a larger optical fiber aperture in order to collect more light signal. The bottom x-y and z scanners are used so that the electron beam position is fixed relative to the tip at about  $1\ \mu\text{m}$  perpendicular to the scan direction. The first NSOM signal is shown in Figure 46. Relative to the figure, the scan direction is from left to right. The corresponding SEM image of the area being scanned is shown in Figure 47. The wires being scanned are on the order of 500 nm in diameter (sample A). The NSOM peaks and wires in the SEM image do not match exactly, primarily due to the displacement of the beam and the NSOM tip.

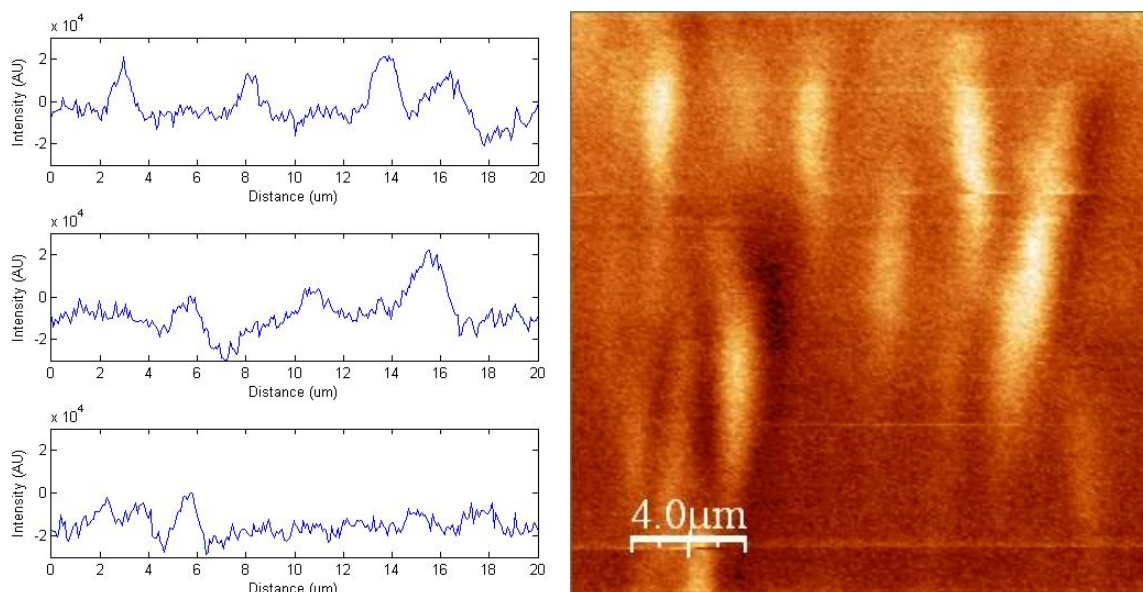


Figure 46. NSOM signals of a group of ZnO nanowires (20  $\mu\text{m}$  x 20  $\mu\text{m}$ ) and representative horizontal intensity line scans.

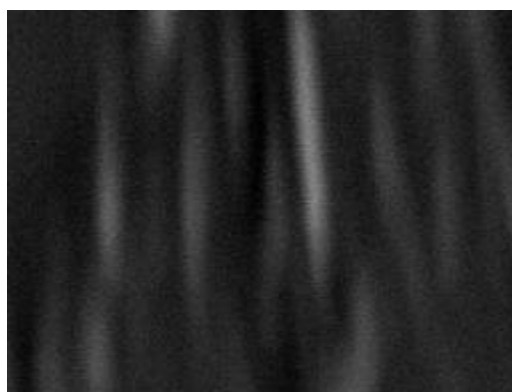


Figure 47. SEM image of the area being scanned for NSOM signal (10000X).

The line scans in Figure 46 show intensity peaks that correlate to the center of the wires. If we consider the wire to be round across its cross-section, then the edge over which the tip must pass is relatively steep. The lateral rate of variation in the intensity over the edge is approximately 600 nm. This provides an estimation of the edge resolution of  $\sim 500$  nm for the tip. Figure 48 shows similar

results with the edge resolution at about  $\sim 550$  nm. These scans were taken in an area where many individual wires are clustered together, hence the broad intensity peaks.

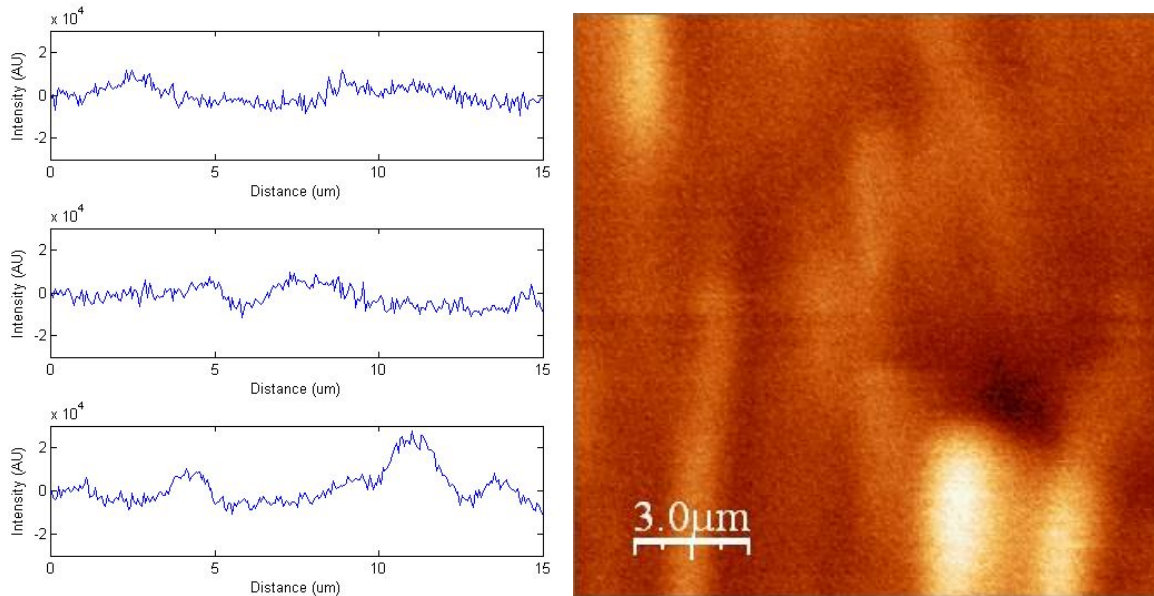


Figure 48. NSOM signals of a 2nd group of ZnO nanowires ( $15 \mu\text{m} \times 15 \mu\text{m}$ ) and representative horizontal intensity line scans.

With these promising results, a 150 nm NSOM tip was used to image higher resolution NSOM nanowire images. The bottom scanner was used again for the x-y and z movement. The area being scanned has a high concentration of smaller wires, ranging from under 100 nm to 200 nm in diameter. Some even smaller wires are lumped together and look like thicker ones. For this measurement, the electron beam was brought as near as possible to the tip at less than 1  $\mu\text{m}$ . Figure 49 shows sharp NSOM intensity peaks over the wires.

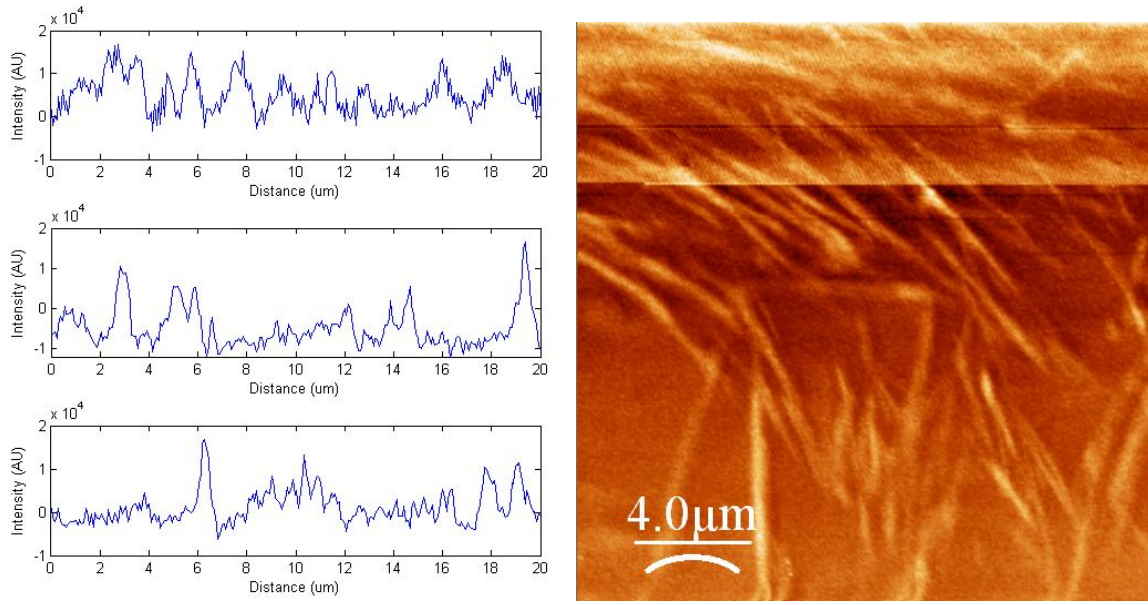


Figure 49. NSOM signals of a ZnO nanowires cluster with much smaller wires (20  $\mu\text{m}$  x 20  $\mu\text{m}$ ) and representative horizontal intensity line scans. The NSOM tip used is 150 nm in diameter.

The intensity profiles from the line scans show the edge resolution estimated at about 200 nm. This is expected, as the NSOM tip (fiber aperture) is significantly smaller. The discontinuity of the NSOM signal shown on the top third of Figure 49 is the result of the electron beam interacting with the tip. The intensity saturation is caused by the beam hitting the tip, charging the tip even more and producing a direct luminescence signal in the fiber.

### C. FIRST DIFFUSION LENGTH MEASUREMENT USING NSOM

The problem of NSOM tip and electron beam interaction prevents the precise imaging of transport with the first generation system. However, by displacing the fixed electron beam some distance away from the NSOM tip and allowing the tip to scan away from the beam, partial imaging of the intensity distribution can be achieved. There are other difficulties associated with this experiment. Firstly, the longer the wires are exposed to electron beam, the less the luminescence they will emit. Secondly, the charges on the NSOM fiber tip

accumulate while it is exposed to the electron beam, hence increasing their interaction. For this experiment, we had to use a 'fresh' wire. The 150 nm NSOM tip was used and was optimized for AFM/NSOM scan. The experiment was set up such that the tip (top scanner) scans away from the fixed electron beam and the sample, shown in Figure 50.

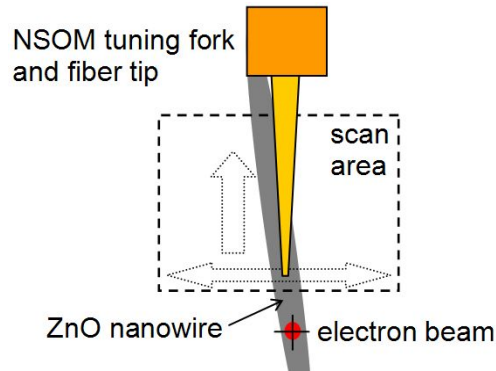


Figure 50. Schematic diagram of the scanning area and beam-tip displacement.

The initial distance of the tip to the electron beam is estimated at 500 nm (any closer than that will saturate the intensity). The electron beam current is  $3 \times 10^{-10}$  A (beam energy is 20 keV), which means the generation region is estimated at 126 nm [21]. Figure 51 shows the results of AFM and NSOM scan. Note that electron beam is approximately 500 nm from the bottom of the images in Figure 51. The NSOM signal clearly shows a rapid decay of intensity along the wire.

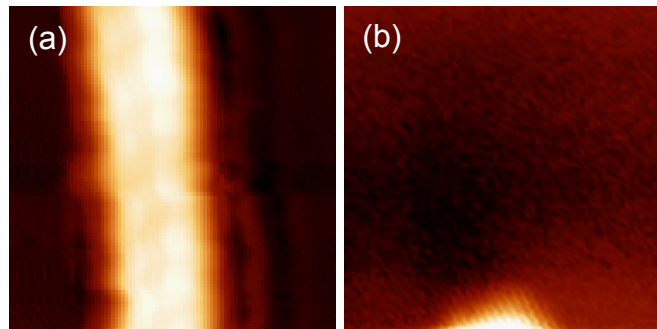


Figure 51. (a) AFM and (b) NSOM scans of a ZnO nanowire ( $2 \mu\text{m} \times 2 \mu\text{m}$ ). The electron beam is approximately  $0.5 \mu\text{m}$  below the two pictures.

The NSOM signal in Figure 51b is analyzed in a line scan along the direction of decay. Figure 52 shows the normalized intensity distribution in both linear and semilogarithmic plots. On the x-axis, the zero point represents the start of the scan. Taking into the account of the beam displacement, the zero point of  $x$  should be approximately  $0.5 \mu\text{m}$ . The region on the semilogarithmic plot where the slope is extracted is from  $0.1 \mu\text{m}$  to  $0.4 \mu\text{m}$ . Using linear regression on these data points, the diffusion length,  $L$  (inverse slope), is  $0.15 \mu\text{m}$ , or  $150 \text{ nm}$ .

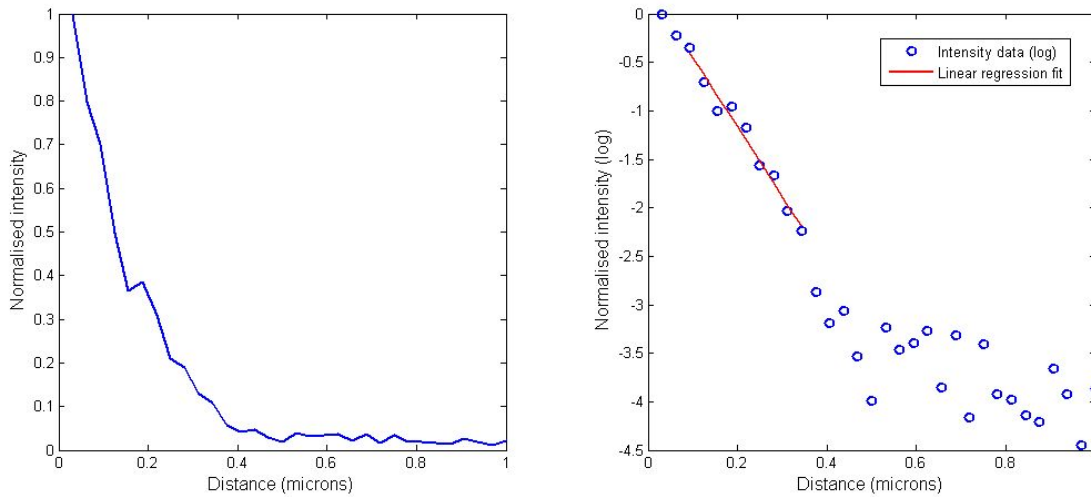


Figure 52. Intensity line scan (linear and semilogarithmic plots) of ZnO NSOM signal along the wire.

This value of  $L$  is within the hypothesis of a ZnO nanostructure diffusion length. The  $L$  is on the order of NSOM tip resolution, the electron beam size and the gap between the tip and the electron beam. Therefore, experiments that are more precise are required to verify the result. This can only be done if the tip and beam interaction problem is solved to bring the scanning as close as possible to the electron beam without charge induced drifting.

For very short diffusion length such as ZnO, an electric bias can be applied. The drift due to the presence of the electric field will allow for imaging at points further away from the beam spot. If the electric field value is known, the

diffusion length can be extracted. This will be one approach to deal with the experimental problems encountered when the electron beam and NSOM tip are too close.

## **VII. IMAGING OF OTHER WIRES**

### **A. SILICON NANOWIRES**

The current and future trends in electronic components revolve around using optical interconnections. Si based electro-optic devices are used for optical communications. However a nanoscale Si based light emitter which can be integrated in IC chips is lacking. Semiconductor nanowires exhibit favorable properties for light emission, such as, InGaN/GaN nanowire arrays that have enhanced light emission compared to conventional InGaN/GaN LEDs [34]. Since Si is the material of choice commercially, there is significant research interest on emission from Si nanowire.

#### **1. Si Nanowire Bridges in Microtrenches**

The OM and CCD camera were also used to attempt to image luminescence from a concentration of Si wire bridges in microtrenches. The image was taken using a probe current of  $1 \times 10^{-10}$  A and at 20 keV energy in the SEM picture mode. The camera is exposed for 20 secs. It was found that there was no measureable luminescence from the Si wire bridges (Figure 53). The bright region reflects luminescence from the Si pads and the trench (dark region) is the SiO<sub>2</sub>/Si substrate (see Figure 7).

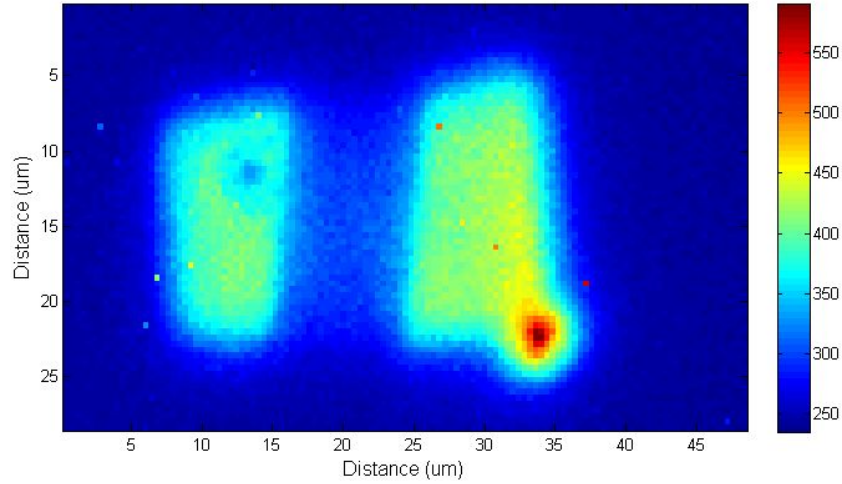


Figure 53. OM image of Si microtrench in SEM picture mode. The wires are in the intermediate regions between the 2 bright spots.

## 2. Si Nanowires Made from CVD

Additional Si wires were provided by HP laboratories. There were 3 different samples used for imaging (Table 4). The 3 samples provided an opportunity to investigate luminescence as a function of 2 parameters: the type of catalyst islands (Au, Ti) and doping.

Sample ID	Catalyst Island	Doping	Wire Diameter
CVD 895	Au	Phosphorus-doped	~ 100 nm
CVD 893	Au	Undoped	~ 100 nm
CVD 904	Ti	Undoped	~ 100 nm

Table 4. HP Si nanowire samples.

The SEM pictures of these Si nanowires are interesting as they stand at about  $72^\circ$  vertically (111 plane). Unfortunately, our experiments using the OM only observed some substrate luminescence. Nothing can be identified with a pattern reflecting the nanowires (Figure 54). Variable temperature measurements to 4.2K were performed in the hope of getting more radiative recombination, but

no luminescence was detected. Again, substrate luminescence was detected. There is no evidence of spatial variation or directionality associated with the wires. Further efforts will be required to produce Si nanowires with detectable luminescence, at these wire diameters of approximately 100 nm.

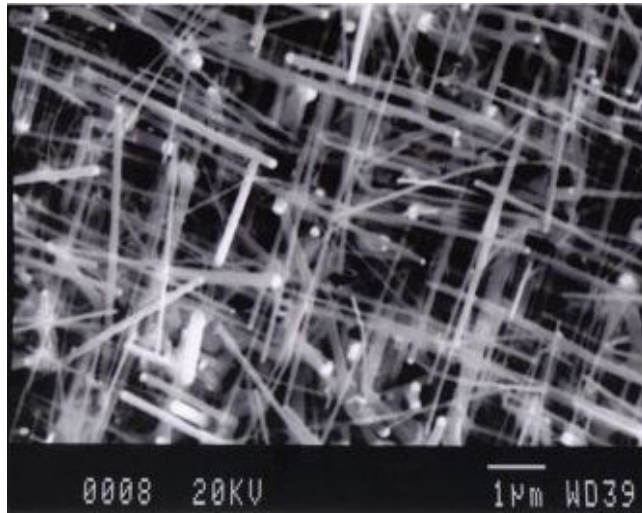


Figure 54. HP sample CVD 895 at 10000X.

THIS PAGE INTENTIONALLY LEFT BLANK

## **VIII. CONCLUSIONS AND SUGGESTIONS FOR FURTHER RESEARCH**

### **A. CONCLUSION**

The work described in this thesis begins the process of extending previous work [6]-[7] in minority carrier transport imaging to the nano-scale regime. In general, by using CL from an SEM, minority carrier transport was imaged using an OM. The work concentrated on nanowires, particularly ZnO nanowires of interest for UV emitters. The wires are on the order of 50 to 200 nm in diameter but relatively long with length of  $\sim 5$  to 10  $\mu\text{m}$ . At this scale, these quasi-1D nanostructures are subject to quantum mechanical and surface scattering effects that complicate the CL process. Additionally, in this nanoscale regime, the OM is fundamentally limited by the optical resolution due to diffraction. To address this issue, an NSOM is required to obtain sub-wavelength resolution.

Using the OM, relatively bigger ZnO wires were imaged. The technique described in this thesis allows the extraction of diffusion length from the intensity profiles using the 1D model (without quantum mechanical effects). In the absence of an externally applied field, the intensity falls exponentially with distance and the inverse slope of the semi-logarithmic plot in the far x region is the diffusion length. The diffusion length of ZnO nanostructures is largely unexplored [31] and hence the results of this work may be the first direct measurements of the parameter.

One key result of this thesis is demonstrating the successful operation of the AFM/NSOM within the SEM. The SEM was used to generate charges and the NSOM was used in place of the OM for transport imaging. Using this unique apparatus, ZnO nanowires were imaged. But the spatial information (intensity distribution due to diffusion/drift) was not captured. This is because the light collection tip and the beam were held fixed while the sample scans in the x-y

plane. The ideal experiment is to fix the electron beam from the SEM on a single wire and let the NSOM tip scan the length of that wire to collect steady-state luminescence spatially. However, with the current tip design, the tip and the beam are interacting due to excess electron charging on the  $\text{SiO}_2$  tip. The charging of the tip causes the electron beam to move in an unpredictable way.

From the results of the thesis work, a method of imaging minority carrier transport in nanostructures is developed. The work demonstrated the feasibility of using near field optical systems within conventional SEM for successful imaging quasi-1D and nanostructures. This lays a foundation for more precise and controlled measurements and is a stepping-stone for developing new techniques to characterize transport properties of nanowires and related nanostructures.

## **B. SUGGESTIONS FOR FURTHER RESEARCH**

### **1 New NSOM Tips**

New NSOM tips will have improved metal coating around the fiberglass tip to reduce the tip-beam interaction. The magnetic catch of the tip mount will also be changed to eliminate astigmatism effects on the electron beam. This will enable the beam to be fixed for the tip to scan freely without affecting it. Thus allows transport imaging along a single wire more precisely without charge-induced drifting of the tip or beam. Then, the diffusion length can be extracted using the collected intensity distribution.

### **2. Applied Electric Field Studies**

The main potential applications of nanowires revolve around optoelectronic devices. Understanding the transport behavior with an electric field behavior is essential. The direct imaging technique presented in this work offers a potential experimental technique for electric field mapping. Current challenges

include coupling contacts to these wires to apply an electric field. By observing the local CL intensity under the influence of an E-field, the magnitude of the field can be observed. Future work should include developing a quantitative method to study the E-field distribution given a material of known parameters.

### **3. Quantum Mechanical and Other Effects in 1D Transport.**

Current work in the thesis looks at wires with diameter greater than 50 nm. Within 50 nm there are ~500 atoms. As Feynman has put it, “There’s plenty of room in the bottom [35]”. Future interests will inevitably be below 50 nm. The low dimensional geometry and nano-scale size will almost certainly give rise to observable changes in minority carrier transport behavior [36]. Further studies are needed to understand the effects of quantum confinement in 2 of the 3 dimensions and as well as other effects associated with smaller sizes. The 1D model could be modified to incorporate these effects and extend the experimental techniques developed in this thesis to explore these new phenomena.

THIS PAGE INTENTIONALLY LEFT BLANK

## ANNEX – MATLAB PROGRAMS FOR DATA ANALYSIS

```
% Cleanpix.m - to filter out single pixel noise in the data array.
% Input: image 2D data, factor
% Output: 'cleaned' 2D image data

function newimg=cleanpix(imgdata,comparefactor)

if nargin < 2
    comparefactor=1.5; % change of 50% tolerance to filter out bad
    pixel
end

newimg=imgdata;
pos=[0,0];
maxvalue=0;

base=findbase(imgdata);

a=size(imgdata);
rowmax=a(1);
colmax=a(2);
pfactor=2;

for i=1:rowmax
    for j=1:colmax
        pos=[i,j];
        if (pos(1)~=1) & (pos(2)~=1) & (pos(1)~=rowmax) &
        (pos(2)~=colmax)
            highpixel=double(imgdata(pos(1),pos(2)));
            lowpixel(1)=double(imgdata(pos(1)-1,pos(2)-1));
            lowpixel(2)=double(imgdata(pos(1)-1,pos(2)));
            lowpixel(3)=double(imgdata(pos(1)-1,pos(2)+1));
            lowpixel(4)=double(imgdata(pos(1)+1,pos(2)-1));
            lowpixel(5)=double(imgdata(pos(1)+1,pos(2)));
            lowpixel(6)=double(imgdata(pos(1)+1,pos(2)+1));
            lowpixel(7)=double(imgdata(pos(1)-1,pos(2)));
            lowpixel(8)=double(imgdata(pos(1)+1,pos(2)));

            avelowpixel=sum(lowpixel)/8;
            pfactor=highpixel/avelowpixel;
        end
        if (pfactor >= comparefactor)
            newimg(pos(1),pos(2))=base;
        end
    end
end

return
```

```

% findbase.m - to find the base noise of a 2D data image
% Input: image 2D data
% Output: the base noise level

function basevalue=findbase(imgdata)

a=size(imgdata);
rowmax=a(1);
colmax=a(2);
b=mean(imgdata);
prevave=round(mean(b));
flag=1;

while flag==1

    for i=1:rowmax
        for j=1:colmax
            if imgdata(i,j)>prevave
                imgdata(i,j)=prevave;
            end
        end
    end

    b=mean(imgdata);
    ave=round(mean(b));

    if ave==prevave
        flag=0;
    else prevave=ave ;

    end
end

basevalue=ave;

return

```

```

% findmax.m - to find the peak of the intensity profile 2D image taking
% into account of bad pixels
% Input: image 2D data
% Output: Row and Column position of maximum point

function pos=findmax(imgdata,base)

pos=[0,0];
maxvalue=0;

comparefactor=0.5; % change of 50% tolerance to filter out bad pixel
a=size(imgdata);
rowmax=a(1);
colmax=a(2);
vfactor=20;
flag=1;

while flag==1
    for i=1:rowmax
        for j=1:colmax

            value=imgdata(i,j);

            if value >= maxvalue
                maxvalue=value;
                pos=[i,j];
            end
        end
    end
    if (pos(1)~=1) & (pos(2)~=1) & (pos(1)~=rowmax) & (pos(2)~=colmax)
        highpixel=double(imgdata(pos(1),pos(2)));
        lowpixel(1)=double(imgdata(pos(1)-1,pos(2)-1));
        lowpixel(2)=double(imgdata(pos(1)-1,pos(2)));
        lowpixel(3)=double(imgdata(pos(1)-1,pos(2)+1));
        lowpixel(4)=double(imgdata(pos(1)+1,pos(2)-1));
        lowpixel(5)=double(imgdata(pos(1)+1,pos(2)));
        lowpixel(6)=double(imgdata(pos(1)+1,pos(2)+1));
        lowpixel(7)=double(imgdata(pos(1)-1,pos(2)));
        lowpixel(8)=double(imgdata(pos(1)+1,pos(2)));
        avelowpixel=sum(lowpixel)/8;
        vfactor=highpixel/avelowpixel;
    end
    if (vfactor >= 1-comparefactor) & (vfactor <= 1+comparefactor)
        flag=0;
    else
        imgdata(pos(1),pos(2))=base;
        maxvalue=0;
    end
end
return

```

```

% slope.m - to find the slope of a linedata using linear regression
% Input: a 1D line data (0.4um/datapoint), center and distance span of
% slope to be taken.
% Output: the slope of the specified region

function gradient=slope(linedata,center,span)

size=length(linedata);
pixcenter=round(center*2.5);
pixindex=round(size/2)+pixcenter;

range=round(size/2)-1;
pixrange=round(range*2.5);
scale=-pixrange:pixrange;
xd=scale*0.4;

pixelspan=round(span*2.5/2);

rstart=pixindex-pixelspan;
rend=pixindex+pixelspan;

x=xd(rstart:rend);
y=linedata(rstart:rend);
lny=log(y);
coef=polyfit(x,lny,1);

gradient=coef(1);

return

```

```

% linecut.m - perform a horizontal or vertical cut on the 2D image data
% and gives a 1D line data
% Input: image 2D data, x-range to cut, position of the intensity peak
% Output: 2D line data

function line=linecutx(imgdata,range,maxpos)

basevalue=findbase(imgdata);

if nargin < 3
    maxpos=findmax(imgdata,basevalue);
end

if nargin < 2
    range=20; %set default range to - 20 to + 20
end

pixrange=round(range*2.5);

imgdata=imgdata-basevalue;
norimgdata=normalise(imgdata,maxpos);
cut=norimgdata(maxpos(1),:); % x-cut
%cut=norimgdata(:,maxpos(2)); % y-cut
line=cut(maxpos(2)-pixrange:maxpos(2)+pixrange);
%line=cut(maxpos(1)-pixrange:maxpos(1)+pixrange);

return

```

```

% slopeadjust.m - To filter out the slant of mounted sample
% Input: topography data
% Output: slope adjusted data

function flatdata=(dataT)

%--get a line and find the slope--
picsize=size(dataT);

pixelx=1:picsize(2);
for a=1:picsize(1)
    linex=dataT(a,:);
    poly=polyfit(pixelx,linex,1);
    slpx(a)=poly(1);
end
slopex=mean(slpx);

pixely=1:picsize(1);
for a=1:picsize(2)
    liney=dataT(:,a);
    liney=transpose(liney);
    poly=polyfit(pixely,liney,1);
    slpy(a)=poly(1);
end
slopey=mean(slpy);

%--use the slope to adjust the image--
picsize=size(dataT);
for i=1:picsize(1)
    for j=1:picsize(2)
        slopebasex(i,j)=j*slopex;
        slopebasey(i,j)=i*slopey;
    end
end

slopebase=(slopebasex+slopebasey);
flatdata=dataT-slopebase;

return

```

## LIST OF REFERENCES

- [1] M.H. Huang, Y. Wu, H. Feick, N. Tran, E. Weber and P.D. Yang, *Catalytic growth of Zinc Oxide Nanowires by Vapor Transport*, Adv. Mater., **13**, No. 2, January 16, 2001.
- [2] R. He, D. Gao, R. Fan, A.I. Hochbaum, C. Carraro, R. Maboudian, P.D. Yang, *Si Nanowire Bridges in Microtrenches: Integration of Growth into Device Fabrication*, Adv. Mater., **17**, 2098, 2005.
- [3] T.I. Kamins, R.S. Williams, Y. Chen, Y.-L. Chang and Y.A. Chang, *Chemical vapor deposition of Si nanowires nucleated by TiSi<sub>2</sub> islands on Si*, Applied Physics Letters, **76**, 5, 2000.
- [4] I. Shalish, H. Temkin and V. Narayanamurti, *Size-dependent Surface Luminescence in ZnO Nanowires*, Physical Review B **69**, 245401, 2004.
- [5] A.T. Tilke et al., *Quantum interference in a one-dimensional silicon nanowire*, Physical Rev. B, vol. **68**, 075311, 2003.
- [6] N.M. Haegel, J.D. Fabbri, and M.P. Coleman, *Direct transport imaging in planar structures*, Applied Physics Letters, **84**, 1329, 2004.
- [7] D.R. Luber, F.M. Bradley, N.M. Haegel, M.C. Talmadge, M.P. Coleman, T.D. Boone, *Imaging Transport for The Determination of Minority Carrier Diffusion Length*, Applied Physics Letters, **88**, 163509, 2006.
- [8] MIT, Internet, <http://web.mit.edu/ISN>, October, 2007.
- [9] B.G. Yacobi and D.B. Holt, *Cathodoluminescence Microscopy of Inorganic Solids*, Plenum Press, New York and London, 1990.
- [10] K. Kanaya and S. Okayama, *J. Appl Phys.* **5**, 43, 1972.
- [11] D.K. Schoroder, *Semiconductor Material and Device Characterization*, Wiley-Interscience, New York, 1990.
- [12] T.E. Everhart and P. H. Hoff, *J. Appl Phys.* **42**, 5837, 1971.
- [13] S.M. Sze, *Semiconductor Devices – Physics and Technology (2<sup>nd</sup> Edition)*, Wiley, USA, 2002.
- [14] Nanosens, Internet, <http://www.nanosens.nl>, October 2007.

- [15] M.T. Sampson, Tiny nanowire could be next big diagnostic tool for doctors, Internet, [http://www.eurekalert.org/pub\\_releases/2003-12/acs-nc121603.php](http://www.eurekalert.org/pub_releases/2003-12/acs-nc121603.php), October 2007.
- [16] Materials for Micro- and Nanosystems (MMNS), Internet, <http://mmns.epfl.ch/page62572.html>, October, 2007.
- [17] B. Xiang, et al., *Rational Synthesis of P-type Zinc Oxide Nanowire Arrays Using Simple Chemical Vapor Deposition*, *Nano Letters*, online, December 29, 2006.
- [18] L.I. Rugani, PHOTONICS, Periodical , p.117, Laurin Publications, September 2007.
- [19] K.v. Klitzing, G. Dorda, and M. Pepper, *New Method for High-Accuracy Determination of the Fine-Structure Constant Based on Quantized Hall Resistance*, *Phys. Rev. Lett.* 45, 494-497, 1980.
- [20] R. Landauer, *Conductance determined by transmission: probes and quantised constriction resistance*, *J. Phys.: Cond. Matter* 1, 8099, 1989.
- [21] S. D. Winchell, *Transport in the one Dimensional Limit*, Master's Thesis, Naval Postgraduate School, Monterey, California, Jun 2006.
- [22] P. Andrikopoulos, *Direct Electric Field Visualization in Semiconductor Planar Structures*, Master's Thesis, Naval Postgraduate School, Monterey, California, Dec 2006.
- [23] L. F. Pedrotti, L.S. Pedrotti and L.M. Pedrotti, *Introduction to Optics – Third Edition*, Pearson Prentice Hall, New Jersey, 2007.
- [24] Photonics.com, *Resolution of Fluorescing Microscope Reaches 15nm*, Internet, <http://www.photonics.com/content/news>, October, 2007.
- [25] M. Born and E. Wolf, *Principles of Optics – Seventh (expanded) Edition*, Cambridge University Press, 1999.
- [26] Wikipedia public domain image, <http://en.wikipedia.org/wiki/Image:Airy-pattern.png>, October 2007.
- [27] Olympus, *Microscopy Resource Center*, Internet, <http://www.olympusmicro.com>, September, 2007.
- [28] A. D L. Humphris, M. J. Miles, J. K. Hobbs, *A mechanical microscope: High-speed atomic force microscopy*, *Appl. Phys. Lett.* **86**, 034106, 2005.

- [29] Nanonics, *Multiview 2000<sup>TM</sup>*, Internet, <http://www.nanonics.co.il>, September, 2007.
- [30] Nanonics, *Multiview 2000<sup>TM</sup> user manual*, version D, March 2007.
- [31] O. Lopatiuk, A. Osinsky, L. Chernyak, *Minority Carrier Transport in ZnO and Related Materials*, Chapter 6, *ZnO Bulk, Thin Films and Nanostructures*, Elsevier, 2006.
- [32] Y. N Yong, X. Cheng, S. Henning, J.I. Sohn, W.E. Welland, D.J. Kang, *Ink-jet printed ZnO nanowire field effect transistors*, Appl. Phys. Lett. 91, 043109, 2007.
- [33] M. Labardi, P.G. Gucciardi, M. Allegrini, C. Pelosi, *Assessment of NSOM resolution on III-V semiconductor thin films*, Appl. Phys. A, **66**, S397–S402, 1998.
- [34] H. M. Kim et al, *High-Brightness Light Emitting Diodes Using Dislocation-Free InGaN/GaN Multiquantum-Well Nanorod Arrays*, Nano Lett. **4**, 1059, 2004.
- [35] R. Feynman, '*There's Plenty of Room at the Bottom*', Speech, Annual Meeting of the American Physical Society, Caltech, December 29, 1959.
- [36] D.K. Ferry and S.M. Goodnick, *Transport in Nanostructures*, Cambridge University Press, 2001.

THIS PAGE INTENTIONALLY LEFT BLANK

## INITIAL DISTRIBUTION LIST

1. Defense Technical Information Center  
Ft. Belvoir, Virginia
2. Dudley Knox Library  
Naval Postgraduate School  
Monterey, California
3. Professor James H. Luscombe  
Chairman, Department of physics  
Naval Postgraduate School  
Monterey, California
4. Professor Nancy M. Haegel  
Naval Postgraduate School  
Monterey, California
5. Ang Goon Hwee  
Republic of Singapore Navy  
Singapore, Singapore